

Upper tropospheric slightly ice-subsaturated regions: Frequency of occurrence and statistical evidence for the appearance of contrail cirrus

Yun Li^{1,2}, Christoph Mahnke¹, Susanne Rohs¹, Ulrich Bundke¹, Nicole Spelten², Georgios Dekoutsidis³,
5 Silke Groß³, Christiane Voigt^{3,4}, Ulrich Schumann³, Andreas Petzold¹ and Martina Krämer^{2,4}

¹Forschungszentrum Jülich, Institute of Energy and Climate Research – Troposphere (IEK-8), Jülich, Germany

²Forschungszentrum Jülich, Institute of Energy and Climate Research – Stratosphere (IEK-7), Jülich, Germany

³Deutsches Zentrum für Luft- und Raumfahrt (DLR), Institut für Physik der Atmosphäre, Oberpfaffenhofen, Germany

⁴Johannes Gutenberg-Universität, Institute of Atmospheric Physics, Mainz, Germany

10 *Correspondence to:* Yun Li (yun.li@fz-juelich.de) and Martina Krämer (m.kraemer@fz-juelich.de)

Abstract. Microphysical, optical and environmental properties of contrail cirrus and natural cirrus were investigated by applying a new, statistically based contrail–cirrus separation method to 14.7 h of cirrus cloud measurements (sampling frequency 1 Hz, max. ~ 290 m/s, total length of sampled in-cloud space ~ 15000 km) during the airborne campaign ML-CIRRUS in Central Europe and the Northeast Atlantic flight corridor in Spring 2014. We find that pure contrail cirrus appears
15 frequently at the aircraft cruising altitude (CA) range with ambient pressure varying from 200 to 245 hPa. They exhibit a higher median ice particle number concentration (N_{ice}), a smaller median mass mean radius (R_{ice}), and lower median ice water content (IWC) (median: $N_{ice} = 0.045 \text{ cm}^{-3}$, $R_{ice} = 16.6 \text{ }\mu\text{m}$, $IWC = 3.5 \text{ ppmv}$), and they are optically thinner (median extinction coefficient $Ext = \sim 0.056 \text{ km}^{-1}$) than the cirrus mixture of contrail cirrus, natural in situ-origin and liquid-origin cirrus found
20 around the CA range (median: $N_{ice} = 0.038 \text{ cm}^{-3}$, $R_{ice} = 24.1 \text{ }\mu\text{m}$, $IWC = 8.3 \text{ ppmv}$, $Ext = \sim 0.096 \text{ km}^{-1}$). The lowest and thickest cirrus, consisting of a few large ice particles, are identified as pure natural liquid-origin cirrus (median: $N_{ice} = 0.018 \text{ cm}^{-3}$, $R_{ice} = 42.4 \text{ }\mu\text{m}$, $IWC = 21.7 \text{ ppmv}$, $Ext = \sim 0.137 \text{ km}^{-1}$). Furthermore, we observe that, in particular, contrail cirrus occurs more often in slightly ice-subsaturated instead of merely ice saturated to supersaturated air as often assumed, thus indicating the possibility of enlarged contrail cirrus existence regions. The enlargement is estimated, based on IAGOS long-term observations of relative humidity with respect to ice (RH_{ice}) aboard passenger aircraft, to be approximately 10% for Europe and the North
25 Atlantic region with the RH_{ice} threshold for contrail cirrus existence decreased from 100% to 90% RH_{ice} and a 4-hour lifetime of contrail cirrus in slight ice-subsaturation assumed. This increase may not only lead to a non-negligible change in contrail cirrus coverage and radiative forcing but also affect the mitigation strategies of reducing contrails by rerouting flights.

1 Introduction

The global aviation sector makes up approximately 5% of anthropogenic global warming (Grewe et al., 2021; Klöwer et al.,
30 2021). Contrail cirrus is one of the largest radiative forcing components of aviation (Lee et al., 2009; 2021) with uncertainties

arising from many sources, including limited knowledge of cirrus cloud properties, spatial coverage and life cycle (Schumann and Heymsfield, 2017; Kärcher, 2018; Burkhardt et al., 2018). Contrail cirrus comprises line-shaped contrails in the wake of high-flying aircraft and thin cirrus patches resulting from the dispersion of long-living contrails. Only a few models account for the water emitted from the aircraft causing contrails in slightly subsaturated air and for the ice water content in contrails during their life cycle extending their persistence (Schumann, 2012). Instead, models often estimate contrail cirrus coverage based on simplified contrail ageing and spreading mechanisms in ice-supersaturated regions (ISSRs) (Burkhardt et al., 2010; Burkhardt and Kärcher, 2011).

Contrails form when hot and humid aircraft exhaust mixes rapidly with cold and humid ambient air so that the humidity in the exhaust gases exceeds liquid water solution (Appelman, 1953; Schmidt, 1941; Schumann, 1996). In such air supersaturated with respect to liquid water ($RH_w > 100\%$), aerosol particles emitted from the aircraft (combustion soot and sulphuric acid-water droplets) or pre-existing in the in-mixed ambient air become activated to form water droplets that freeze subsequently to contrail ice particles. According to the purely thermodynamic Schmidt-Appelman criterion (SAC), the threshold temperature for contrail formation depends on ambient air pressure and humidity, on the amount of water and heat emitted by the aircraft per fuel mass and on the aircraft engine's overall propulsion (Schumann, 1996; Jensen et al., 1998). After reaching the ambient temperature by mixing with the surrounding air, the contrails grow or shrink in size depending on ambient humidity. If the ambient relative humidity remains supersaturated with respect to ice ($RH_{ice} > 100\%$), contrails grow in ice water content and can persist for up to 5 h or even longer (Gierens and Vázquez-Navarro, 2018; Schumann and Heymsfield, 2017), and may spread and evolve into thin cirrus layers. Otherwise, contrail ice particles sublime and dissipate on a timescale dependent on their size and the ambient air RH_{ice} (Schumann, 2012).

A robust estimation of contrail cirrus' radiative effect depends largely on their optical properties (related to their microphysical properties and age) and geographical appearance. Young contrails can exert an instantaneous radiative forcing to warm and cool the atmosphere that is three orders of magnitude larger than their net warming effect (Gierens et al., 2020). The microphysical features of contrail cirrus at different plume ages observed from various airborne campaigns were compiled and described in Schröder et al. (2000), Schumann et al. (2017) and Chauvigné et al. (2018). Fresh contrails are characterised by an ice crystal number concentration (N_{ice}) of thousands of ice crystals per cubic centimetre in size up to a few micrometres in diameter, as observed in an approximately 2-minute-old plume (Petzold et al., 1997). Two to five minutes old contrails were frequently measured (*e.g.* Voigt et al., 2011; Gayet et al., 2012). Here, contrail ice crystal number concentrations were diluted to 100 to 400 per cubic centimetre and ice crystal diameters increased to 4 to 10 μm due to condensational growth (Jeßberger et al., 2013; Bräuer et al., 2021). Slightly older contrails at a maximum plume age of 30 minutes dilute further by the inmixing of ambient air down to less than hundreds of ice crystals that have grown to tens of micrometres (Schröder et al., 2000). The peculiar high N_{ice} of small ice particles makes young contrails easy to be distinguished from natural cirrus. At an even later stage, N_{ice} of contrail cirrus further decreases significantly to a few ice particles per cubic centimetre or less, with particle sizes being 2–3 orders of magnitude larger, becoming similar to natural cirrus and making the discrimination between contrail and natural cirrus difficult. Contrail cirrus are generally characterized by low ice water content (IWC) ranging from 0.1 to about

65 10 mg/m³ (Schumann et al., 2017), like natural cirrus of in situ-origin whose ice crystals have formed and grown in an ice cloud only environment (Luebke et al., 2016; Krämer et al., 2020). Different from contrail cirrus and in situ-origin cirrus, liquid-origin cirrus often yield higher IWC (Krämer et al., 2016; Krämer et al., 2020) because their ice crystals originally form as liquid drops in a warmer atmosphere ($T_{\text{amb}} > 235 \text{ K}$), which subsequently freeze while being lifted into the cirrus temperature region of the atmosphere.

70 The fact that contrails often coexist with natural cirrus and become embedded within thin or subvisible cirrus (Kübbeler et al., 2011; Gierens, 2012; Unterstrasser, 2017) makes it challenging to discriminate between aged contrails and natural cirrus, thus impeding clarifying contrail cirrus' contribution to the radiative balance. Chauvigné et al. (2018) has employed a principal component analysis method to distinguish between contrail cirrus particles at different ages and natural cirrus measured during the CONCERT 2008 campaign (Voigt et al., 2010), which is successful because contrails sampled during the CONCERT
75 campaign were rather young and more recognisable compared to natural cirrus. However, not all required optical and microphysical parameters can be obtained from single aircraft campaigns to apply this method widely, and the CONCERT dataset is small, around 4.0 h of contrail and natural cirrus sampling time in total (Kübbeler et al., 2011).

A common assumption on the conditions for contrail cirrus formation and evolution is that contrail cirrus occurs and persists merely in ISSRs (Kärcher, 2018). In fact, contrails and contrail cirrus were also observed in ice-subsaturated air not only during
80 contrail-dedicated research flights (Kübbeler et al., 2011; Voigt et al., 2011; Gayet et al., 2012; Schumann et al., 2017; Chauvigné et al., 2018) but also from IAGOS commercial aircraft observations in the North Atlantic region (Petzold et al., 2017). Apart from a high number of small contrail ice particles, large particles (ice particle diameter $D_p > 100 \mu\text{m}$) were also detected, but at relatively low concentrations (Voigt et al., 2010; Kübbeler et al., 2011; Chauvigné et al., 2018). Such large ice crystals were also observed in contrail cirrus during the ML-CIRRUS campaign (Voigt et al., 2017). However, attention to
85 contrail cirrus in ice-subsaturated environments and the role that large ice particles play in contrail cirrus was raised only by Kübbeler et al. (2011) and Schumann (2012). Kübbeler et al. (2011) discussed that the subsaturation feature observed in contrail cirrus during the CONCERT campaign is accompanied by the sublimation of those large ice particles, which might be sedimented from higher levels after being formed under ISSRs. As the contrail cirrus dataset is limited to only a few segments of several flights, it could not be corroborated that the existence of contrail cirrus in ice-subsaturated environments is a common
90 feature. But Schumann and Graf (2013) found it necessary to reduce the critical humidity above which contrails form to a value below ice saturation to model contrail occurrence and their longwave radiative forcing in agreement with multi-year satellite observations over the North and South Atlantic.

Currently, the prevalent strategy for contrail avoidance is to reroute the aircraft around ice-supersaturated regions by flying at slightly higher or lower altitudes to avoid contrail formation or minimise contrail radiative forcing (Teoh et al., 2020a; Niklaß
95 et al., 2021). Teoh et al. (2020a) showed that focusing on the avoidance of strong contrails, the so-called big hits, reduces the radiative forcing effect because only for these cases, the “saved” radiative forcing overrules the additional CO₂ emitted during the rerouting of the aircraft. Gierens et al. (2020) showed that the formation of contrails can be predicted with some success, but there are problems in predicting contrail persistence due to limited knowledge about the occurrence of air masses around

ice saturation. Particularly from this study, it becomes evident that further knowledge about the distribution of air masses around ice saturation and the resulting properties of aircraft-induced cirrus and natural cirrus is required (Teoh et al., 2022). In this study, we investigate a larger dataset of 14.7 h cirrus cloud sampling (frequency 1 Hz, max. ~ 290 m/s) obtained during the ML-CIRRUS 2014 campaign (Sect. 2.1) than the 4-hour CONCERT dataset. With commonly available parameters describing the microphysical properties of cirrus, such as N_{ice} , ice crystal sizes and IWC, we adopt a simpler statistical approach to separate aviation-induced cirrus from natural cirrus compared with Chauvigné et al. (2018). It consists of the SAC, the most frequent aircraft cruising altitude range and a newly developed aircraft exhaust plume detection algorithm (Mahnke et al., 2022) to differentiate aged contrail cirrus (> 0.5 h lifetime, Schumann et al., 2017; Voigt et al., 2017) and natural cirrus (Sect. 2.3). We show step by step the sharpened differentiation of contrail cirrus from natural cirrus and report on their microphysical properties and occurrence conditions (Sect. 3.1–3.2). In addition, we analyse the humidity of the environments of contrail and natural cirrus (Sect. 3.3). Based on these observations, we simulate the lifetime of ice particles that have similar microphysical properties to the contrail cirrus sampled during ML-CIRRUS in slightly ice-subsaturated environments. Furthermore, we inspect 15 years of RH_{ice} measurements aboard passenger aircraft in the IAGOS global monitoring framework to shed light on how the existence of contrail cirrus in environments with $RH_{\text{ice}} \geq 90\%$ might influence contrail mitigation (Sect. 4).

2 Datasets and methods

2.1 ML-CIRRUS dataset

The Mid-Latitude CIRRUS (ML-CIRRUS) campaign was conducted from Oberpfaffenhofen, Germany to probe cirrus clouds over Central Europe and the Northeast Atlantic region in March and April 2014 (Voigt et al., 2017). The High Altitude and Long-Range Research Aircraft (HALO, Krautstrunk and Giez, 2012) was deployed to investigate the formation mechanism, life cycle and climate impact of natural cirrus and aircraft-induced cloudiness. Excluding test flights and the ones with strong instrumental issues, 12 of 17 research flights with the focus on natural and contrail cirrus, as listed in Table S1, are considered here for studying the microphysical properties of contrail cirrus and mid-latitude natural cirrus, which serve as the basis to distinguish contrail cirrus from natural cirrus.

The ML-CIRRUS dataset (Voigt et al., 2017) includes the parameters important for cloud characterisation — in situ relative humidity with respect to ice RH_{ice} , ice water content IWC, ice particle number concentration N_{ice} and mass mean radius R_{ice} . The in situ RH_{ice} was calculated using water vapour mixing ratios measured by the tuneable diode laser hygrometer SHARC (Meyer et al., 2015), ambient temperature T_{amb} and pressure measurements provided by the Basis Halo Measurement and Sensor System (BAHAMAS) (Mallaun et al., 2015; Giez et al., 2017). The overall uncertainty of SHARC H_2O measurement is 5% relative and ± 1 ppm absolute offset uncertainty (Kaufmann et al., 2018). The nominal accuracies of the BAHAMAS pressure and T_{amb} measurement are 0.3 hPa and 0.5 K (Mallaun et al., 2015; Giez et al., 2017; Kaufmann et al., 2018). The overall accuracy of the in-situ RH_{ice} measurements here is between 10 – 20%, with the respective uncertainties of the temperature, pressure and water vapour measurements considered (Krämer et al., 2016). The in situ RH_{ice} , water vapour and

temperature measurements were compared with other instruments on board and model data from the European Centre of Medium-range Weather Forecasting (ECMWF) by Kaufmann et al. (2018). No systematic instrument bias in either water vapour or temperature was identified in the upper troposphere. A further discussion on the reliability of the RH_{ice} measurements can be found in the supplementary material (Sect. S3).

135 Cloud measurements were performed using cloud spectrometer NIXE-CAPS (New Ice eXperiment: Cloud and Aerosol Particle Spectrometer, later referred as NIXE) at a time resolution of 1 Hz (max. ~ 290 m/s) with the instrument mounted under the aircraft wing (Krämer et al., 2016; Luebke et al., 2016). As a combination of the two instruments NIXE-CAS-DPOL (Cloud and Aerosol Spectrometer with Detection of POLarization) and NIXE-CIPg (Cloud Imaging Probe — grayscale), NIXE measures N_{ice} in the particle diameter (D_p) range of $0.61\text{--}937\text{ }\mu\text{m}$, with D_p meaning optical equivalent diameter for CAS-DPOL and area equivalent diameter for CIP-Grayscale, respectively. Only particles of $D_p > 3\text{ }\mu\text{m}$ are considered for cloud measurements, while smaller particles are classified as aerosols. In fresh contrails, particle sizes can be smaller than $3\text{ }\mu\text{m}$, but for consistency and comparability, the lower threshold $D_p = 3\text{ }\mu\text{m}$ is maintained in the analysis of contrails and contrail cirrus. NIXE gives a total uncertainty of $\pm 20\%$ (Meyer, 2012) in particle number concentration measurement. IWC is derived from the ice particle size distribution (PSD_{ice}) in the D_p range of $3\text{--}930\text{ }\mu\text{m}$. How the IWC is determined from a mass-dimension relation and the robustness of the IWC have been stated in Krämer et al. (2016), Luebke et al. (2016) and Afchine et al. (2018). 145 The lower IWC detection limit of NIXE is 0.15 ppmv (parts per million by volume). The ice crystal mass mean radius R_{ice} in μm is calculated with $R_{ice} = 10^4 \times \left(\frac{10^{-6} \times IWC}{N_{ice}} \times \frac{3}{4\pi\rho} \right)^{1/3}$, where IWC is in mg/m^3 (converted from IWC in ppmv), ρ is 0.92 g cm^{-3} and N_{ice} is the total number concentration of ice crystals ($D_p > 3\text{ }\mu\text{m}$) in cm^{-3} . Additional parameters for discriminating contrail and natural cirrus are total aerosol particle number concentration, total 150 reactive nitrogen NO_y mixing ratio and airborne lidar RH_{ice} . Here, the measurements are summarised below (see Voigt et al., 2017 for details).

The total aerosol particle number concentration was measured by the instrument AMETYST (Voigt et al., 2017), which is a combination of four condensation particle counters (CPCs) measuring total and non-volatile aerosols in the size range of $4\text{ nm--}2\text{ }\mu\text{m}$. The uncertainty of the CPCs of AMETYST is in the typical CPC uncertainty range, which is estimated to be of the order of 10% (Petzold et al., 2011; 2013). NO_y was measured by the instrument AENEAS (Ziereis et al., 2000) by catalytically 155 converting NO_y to nitrogen monoxide NO on a gold surface heated at $300\text{ }^\circ\text{C}$. The converted NO will then be directly detected with chemiluminescence technique. AENEAS has an NO_y detection range of 5 parts per trillion by volume (pptv) to 60 parts per billion by volume (ppbv) (Voigt et al., 2017), with an overall uncertainty of 30% or 40 pptv .

The airborne lidar RH_{ice} is derived from water vapour measurement in the 935 nm absorption band of H_2O by the lidar WALES 160 and ambient temperature from ECMWF (Wirth et al., 2009; Groß et al., 2014). For retrieving cirrus clouds from the remote-sensing technique, only the particles producing a back-scattering ratio (BSR) greater than 3 and having a depolarisation ratio greater than 20% at $T_{amb} < 235\text{ K}$ are interpreted as cirrus cloud particles (Urbanek et al., 2018). Note that SHARC measures water vapour concentrations at aircraft positions, WALES obtains atmospheric cloud columns with its laser penetrating through

clouds from the cloud top or bottom. The two instruments do not measure water vapour in parallel. Therefore, the in situ RH_{ice} and lidar RH_{ice} are not from the same clouds. However, the intercomparison of in situ and lidar RH_{ice} measurements inside cirrus clouds promotes the evaluation of the robustness of the in situ RH_{ice} dataset and uncertainties related to the quality of the T_{amb} dataset.

2.2 RH_{ice} dataset from IAGOS passenger aircraft

The RH_{ice} dataset spanning from 1995 to 2010, based on the Measurement of Ozone and Water Vapour on Airbus In-service Aircraft (MOZAIC) programme, is used for the analysis of the RH_{ice} distribution in air masses in the northern mid-latitudes. The MOZAIC programme (Marenco et al., 1998) was initiated in August 1994 and was carried on within the new European Research Infrastructure IAGOS (In-service Aircraft for a Global Observing System, <https://www.iagos.org/>) in 2011 (Petzold et al., 2015). The measurement of atmospheric trace gases and aerosol particles is conducted by autonomous instruments installed on commercial passenger aircraft. Up to now, over 63,000 flights contribute to a global-scale dataset of water vapour and RH_{ice} in the upper troposphere and lower stratosphere (Petzold et al., 2017; Petzold et al., 2020; Reutter et al., 2020). The dataset used for this study has aerial boundaries of 40° – 60° N covering the North Atlantic (65° – 5° W) and Europe (5° W– 30° E). It contains temperature, pressure and RH_{ice} measurements. RH_{ice} is directly measured by the IAGOS Capacitive Hygrometer (ICH). The details regarding the principles of the ICH sensor and sensor calibration as well as the procedures to determine the ambient air temperature from the sensor temperature can be found elsewhere (Neis et al., 2015; Smit et al., 2014). The ICH sensors are usually calibrated before being deployed in the airplane and after deployment. During the deployment period (3–6 months), the sensor output signal in voltage may drift. Therefore, an in-flight calibration method is applied to the reanalysis data to overcome the drifts of sensor signals, thus, to correct erroneous RH_{ice} values (Smit et al., 2008). The overall uncertainty of IAGOS RH_{ice} is about 5% (2–8%) at 10–12 km at cruising altitudes with a detection limitation of $\sim 10\%$ RH_{ice} (Petzold et al., 2020; Smit et al., 2014). The MOZAIC RH_{ice} dataset has been quality checked, successfully validated against RH_{ice} observations by high-precision instruments aboard research aircraft. and also compared to ERA-Interim reanalysis data (Dee et al., 2011) to be reliable for scientific studies (Neis et al., 2015; Petzold et al., 2020; Reutter et al., 2020). The same dataset was described in detail in the study of ice-supersaturated air masses in the northern mid-latitudes (Petzold et al., 2020). Here, the occurrence fractions of air masses at different RH_{ice} thresholds are determined for the North Atlantic region and Europe from this dataset and utilized for the discussion about the potential influence on contrail avoidance (Sect. 3.5).

2.3 Contrails and contrail cirrus detection

Data suitable for statistically analysing the microphysical properties of cirrus induced by aircraft emissions or by atmospheric dynamic systems should meet the following criteria:

1. ambient pressure $p < 350$ hPa, which constrains the pressure altitude to be higher than ~ 8.1 km under standard atmospheric conditions. This is also the common cruising altitude of commercial airplanes.
2. ambient temperature $T_{amb} < 235$ K, which is the cirrus formation temperature region.

2.3.1 The Schmidt-Appleman criterion (SAC)

To determine the potential for contrail formation in the air masses meeting the above thresholds, air mass thermodynamic properties are analysed by applying the Schmidt-Appleman criterion (SAC). The SAC at aircraft pressure level p depends on the gradient G of the mixing line (see Fig. 1) (Schumann, 1996):

$$G = \frac{EI_{H_2O} c_p p}{\varepsilon Q (1 - \eta)}$$

where p is the ambient air pressure, c_p is the isobaric heat capacity of air ($1004 \text{ J kg}^{-1} \text{ K}^{-1}$), ε is the ratio of molar masses of water and dry air (0.622). A water vapour emission index $EI_{H_2O} = 1.25 \text{ kg/kg-fuel}$, fuel heat capacity $Q = 43.2 \text{ MJ/kg-fuel}$ for convectional jet fuel (kerosene) and the overall propulsion efficiency $\eta = 0.31$ are applied to the calculation. G (unit: Pa K^{-1}) represents the gradient of the trajectory of aircraft exhaust air isobaric mixing with the surrounding ambient air — the blue

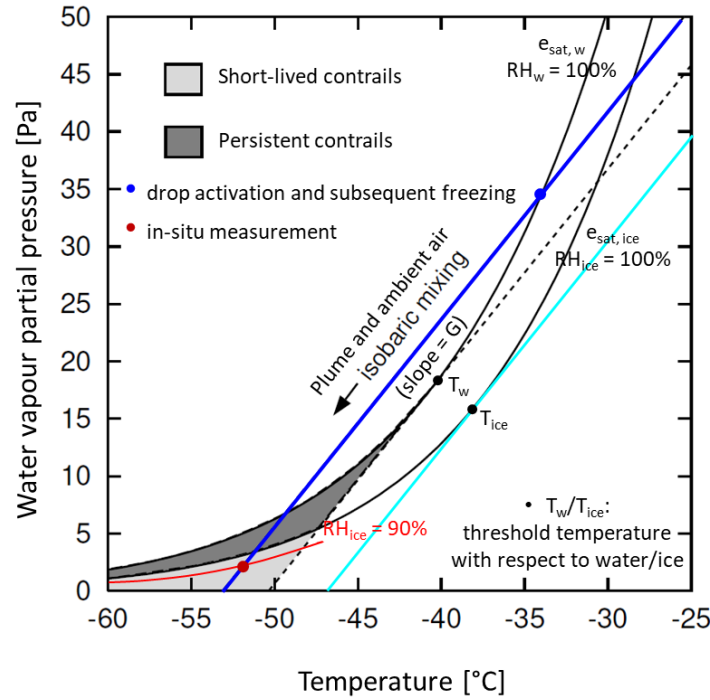


Figure 1. Water vapour saturation partial pressure with respect to liquid water ($e_{\text{sat}, w}$) and ice ($e_{\text{sat}, \text{ice}}$) as a function of temperature. The blue line represents the isobaric mixing of the aircraft exhaust plume with the surrounding ambient air at a gradient of G along the black arrow. During the isobaric mixing, liquid drops form when surpassing water saturation; the drops freeze subsequently at $\sim 235 \text{ K}$. The red dot represents an in situ measured cloud sample that marks the ending point of the cloud sample's mixing. T_w is the threshold temperature for contrails to form. This occurs when the isobaric mixing line (the dashed line) just touches the water saturation curve. In this case, contrails persist in ice-supersaturated environments and live only shortly in ice-subsaturation, as indicated by the dark and light grey areas, respectively. The cyan line shows a situation where the aircraft exhaust air parcel just reaches ice saturation so that contrail ice particles might form directly from the gas phase heterogeneously or homogeneously at the corresponding ice supersaturation. The red curve at $\text{RH}_{\text{ice}} = 90\%$ represents the proposed lower RH_{ice} threshold of persistent contrails in this work (Section 3.3).

plume and ambient air is illustrated (adapted from Fig. 3 in Schumann (1996)). The sampled air masses are assumed to be released from aircraft engines and have undergone the isobaric mixing process while detraining into ambient air. T_{amb} and RH_{ice} at an assumed measuring position (the red dot in Fig. 1), therefore, mark the ending point of an individual air parcel's mixing line. If the mixing line touched or crossed the ice/liquid saturation curve, *e.g.*, the blue, dashed black or cyan lines in Fig. 1, the measured cloud particle could have been very probably involved in the formation of contrails during its evolution. Cirrus cloud particles sampled at thermodynamic positions not fulfilling SAC are considered irrelevant to contrail formation and are treated as natural cirrus.

2.3.2 The most frequent aircraft cruising altitude (CA) range

To better discriminate between contrail and natural cirrus, we define another criterion by dividing the altitude range of the dataset fulfilling SAC into the most frequent aircraft cruising altitude (CA) range and the altitudes beyond. To determine the CA pressure range, we surveyed the 15 years of IAGOS-MOZAIC pressure measurements over the North Atlantic and Europe regions aboard passenger aircraft. The occurrence probabilities of flight levels per 10-hPa bin are shown in Fig. 2. The most frequently visited atmospheric pressure levels are from 200 to 270 K. However, ice cloud properties at lower altitudes with pressure greater than 245 hPa show distinct behaviour from those at higher altitudes below 245 hPa and seem closer to those observed at positions not fulfilling SAC, implying that they could be natural cirrus or extensively aged contrail cirrus. Hence, the pressure altitude range of 200–245 hPa is adopted as the CA range for the further analysis.

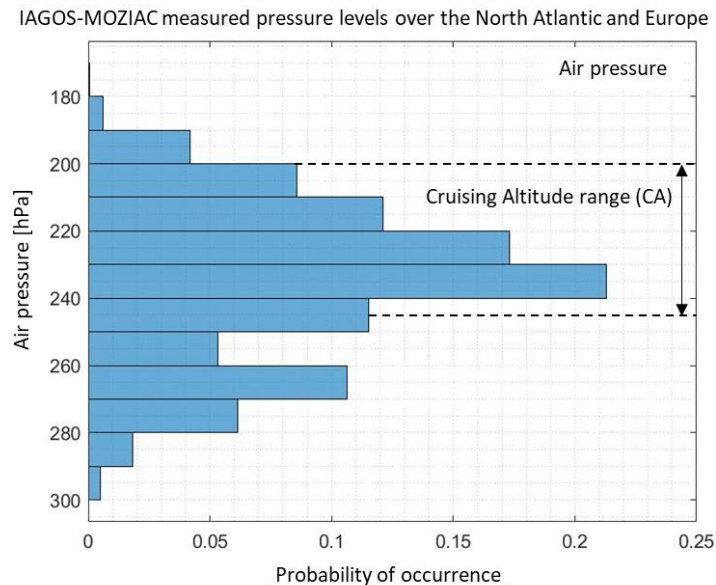


Figure 2. Occurrence fractions of passenger aircraft flight levels in pressure (unit: hPa) measured during the IAGOS-MOZAIC period (1996–2010) over the North Atlantic and Europe. The pressure range 200–245 hPa between the dashed lines is adopted as the most frequent aircraft cruising altitude (CA) range (see text for the determination of the boundary pressure thresholds).

2.3.3 Aircraft plume detection

The principle of the aircraft exhaust plume detection assumes that a simultaneous enhancement of multiple products emitted from aviation fuel combustion, here total aerosol particles and reactive nitrogen NO_y measured by the instruments AMETYST and AENEAS (Sect. 2.1), serves as a clear marker for air masses influenced by aircraft exhaust (Schumann et al., 2002). In this work, the total aerosol particle number concentration and the mixing ratio of NO_y , which can be considered a passive tracer in aircraft plumes up to a plume age of 18 h, are used to detect aircraft exhaust plumes along the flights from the concurrent increased particle number concentrations and NO_y mixing ratios in comparison to atmospheric background values (Mahnke et al., 2022). The plume detection algorithm is restricted to a minimum NO_y excess of around 0.1 ppbv above the atmospheric background, which corresponds to a maximum plume age of approximately 2–5 h, depending on the diffusion speed of aircraft exhaust and NO_y emission index according to aircraft type.

The plume detection algorithm is applied to 10 ML-CIRRUS flights, for which both NO_y and aerosol measurements are available. Only the air masses containing ice particles detected at $T_{\text{amb}} < 235 \text{ K}$ are considered as contrail cirrus. Different from the passive tracer NO_y , cirrus particles are subjected to gravity waves and turbulence. As a result, at some point the contrail ice particles may become spatially separated from the plume and/or the plume may become spatially associated with particles formed in natural cirrus clouds. Therefore, the plume detection algorithm may miss contrail cirrus particles. The contrails that can be found with the help of the plume detection algorithm can be viewed as a subset of the contrails, because as long as the plume is detected and contains cirrus ice particles, these ice particles are highly likely to stem from contrails. The final in-cloud sampling encountered aircraft exhaust plumes as identified by the plume detection algorithm is approximately 0.99 hr, around 3200 cloud samples (max. $\sim 1 \text{ km}$ length of sampled in-cloud space) at 1 Hz sampling frequency. The sizes in flight hours of each sub-datasets after applying the SAC, CA and plume detection criteria are listed in Table S2. We use the plume subset to show that the microphysical properties of these contrails are comparable to those from the larger dataset (determined with SAC+CA) that also includes contrail ice particles spatially separated from the plume. This comparison increases our confidence in the method to identify contrails via the SAC and CA criteria.

3 Properties of contrail and natural cirrus

3.1 Cirrus cloud observations

The full ensemble of cirrus cloud properties (N_{ice} and R_{ice}) observed during ML-CIRRUS as a function of ambient temperature is shown in Fig. 3 together with in situ RH_{ice} . The number of flight hours spent in cirrus clouds is 14.7 h, approximately 15000 km of the sampled in-cloud space in total. Figure 3a and b show the temperature dependence of N_{ice} ($D_p > 3 \mu\text{m}$) and R_{ice} , respectively, binned in 1-K intervals and color-coded by the occurrence frequency that is normalised to the total counts in each temperature interval. One pronounced signature of contrail cirrus is the high $N_{\text{ice}} > 0.1$ or even $> 1 \text{ cm}^{-3}$ between 208–220 K, which could be linked to aviation-induced cirrus (Petzold et al., 2017; Schumann et al., 2017; Krämer et al., 2020) as the

median N_{ice} of the large climatology of cirrus shown by Krämer et al. (2020) is 0.03 cm^{-3} . In the same temperature range, R_{ice} exhibits the highest occurrence frequency at a small mass mean radius around $20 \text{ }\mu\text{m}$ or even lower. The occurrence frequency of N_{ice} in relation to R_{ice} is displayed in Fig. 3c for the whole cirrus dataset with the isolines representing IWC in ppmv, which means that the same IWC could arise from many small ice particles (the upper-left segment of the IWC isolines) or a few large ice crystals (the lower-right segment).

Contrail cirrus often appear in the upper left side of the banana-shaped N_{ice} – R_{ice} relation (Fig. 3c), typical of high N_{ice} , small R_{ice} and low IWC, while natural cirrus more typically cluster in the middle and lower right parts with low N_{ice} , larger R_{ice} and high IWC. The 50th (grey) and 90th (black) percentile contours indicate a pronounced occurrence of contrail cirrus, with IWC mostly below 10 ppmv . The 10 ppmv IWC isoline also roughly sets in situ-origin cirrus apart from liquid-origin cirrus with higher IWC. This classification of cirrus origins was applied to the ML-CIRRUS measurements by Luebke et al. (2016) and is replotted in Fig. S1 (see Supplement), where it can be seen that in situ-origin cirrus appears more frequently with $R_{ice} < 30 \text{ }\mu\text{m}$ and $\text{IWC} < 10 \text{ ppmv}$, while liquid-origin cirrus shows exactly the opposite.

The occurrence frequency of in-cloud RH_{ice} in relation to temperature, as depicted in Fig. 3d, shows one maximum at around $90\% \text{ RH}_{ice}$ in the temperature range of $208\text{--}220 \text{ K}$, which corresponds to the temperature range showing contrail cirrus signals in Fig. 3a and b. The observed occurrence of contrail cirrus in slight subsaturation with respect to ice observed in ML-CIRRUS is consistent with what was reported in Kübbeler et al. (2011) based on the CONCERT dataset. A similar feature is reported from the first analysis of the IAGOS RH_{ice} and cloud dataset in the North Atlantic Flight Corridor for the years 2014 and 2015 (Petzold et al., 2017).

In the following we will discriminate between contrail and natural cirrus and obtain an understanding of the occurrence of contrail cirrus regarding spatial probabilities, cloud properties as well as their favourable atmospheric conditions.

3.2 Cirrus classification

3.2.1 Cirrus differentiated by the Schmidt-Appleman criterion (SAC)

Our attempt at SAC calculation divides the ML-CIRRUS cirrus dataset discussed in the previous section into two categories: the dataset of cloud particles sampled under conditions fulfilling SAC (SAC^+ , $\sim 11.2 \text{ hours}$) and the complementary dataset not fulfilling SAC (SAC^- , $\sim 3.5 \text{ hours}$); see Fig. 1d for details. As discussed in Sect. 2.3.1 and shown in Fig. 1, a cloud sample fulfilling SAC is considered as being very possibly involved in the formation of contrails during its evolution, and the one measured at thermodynamic positions failing SAC is considered irrelevant to contrail formation and is regarded as natural cirrus.

Note, however, that natural cirrus could also be included in the SAC^+ group, meaning that SAC alone is not a sufficient criterion to identify contrail cirrus, while cirrus detected in the SAC^- group can be unambiguously attributed to natural cirrus. Despite the limited differentiation between contrail and natural cirrus by using SAC alone, we will first discuss the differences in the

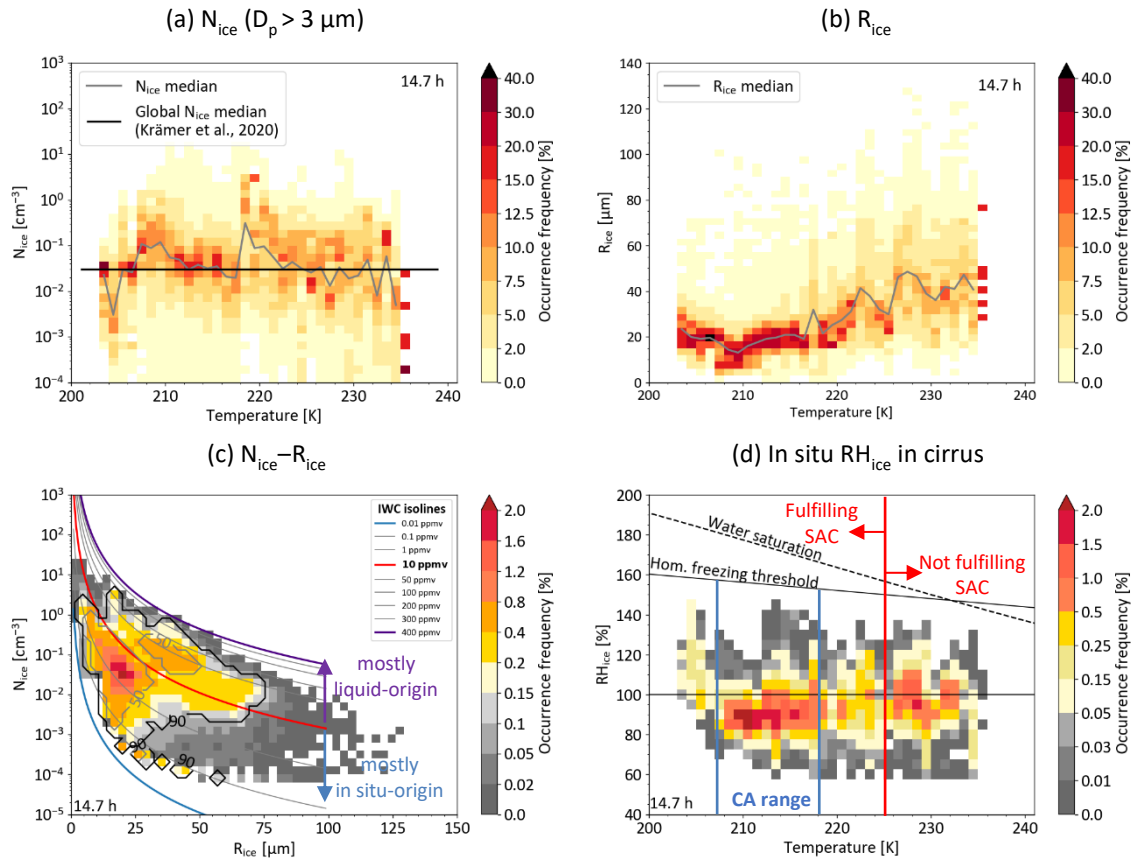


Figure 3. Overview of the cirrus cloud properties measured in Central Europe and the Northeast Atlantic flight corridor during the ML-CIRRUS research aircraft campaign in Spring 2014. (a): Occurrence frequency of ice particle number concentrations (N_{ice}) for all cirrus crystals larger than $3 \mu m$ in diameter (D_p), binned in 1-K intervals. The grey line shows the median N_{ice} in single temperature intervals. The horizontal bar indicates the N_{ice} median from in situ N_{ice} global climatology (Krämer et al., 2020). (b): The same as (a) but for the mass mean radii R_{ice} of cirrus particles. (c): Normalised occurrence frequency of N_{ice} as a function of R_{ice} . Coloured curves are ice water content IWC isolines in parts per million by volume (ppmv). The same amount of IWC could consist of many small ice particles pointing to the left end of the isoline or few large ice crystals to the right end. The grey and black contours enclose 50% and 90% of the most frequently occurring cloud particles. Ice crystals with IWC < 10 ppmv are mostly in situ-origin cirrus, while those with IWC > 10 ppmv are mostly liquid-origin cirrus. (d): Normalised occurrence frequency of in situ RH_{ice} in cirrus clouds. The water saturation (Murphy and Koop, 2005) and homogeneous freezing threshold (Koop et al., 2000) are added. The red vertical line marks the temperature threshold for possible contrail formation, calculated from the Schmidt-Appleman criterion (SAC). The most frequent aircraft cruising altitude boundaries are marked by the blue vertical lines and correspond to a pressure range of 200–245 hPa, 207–218 K.

microphysical properties between the SAC^+ and SAC^- datasets. The sharpening of the separation of the full ensemble into aviation-influenced cirrus and natural cirrus by adding another criterion of the most frequent cruising altitude range will then be discussed in Sect. 3.2.2.

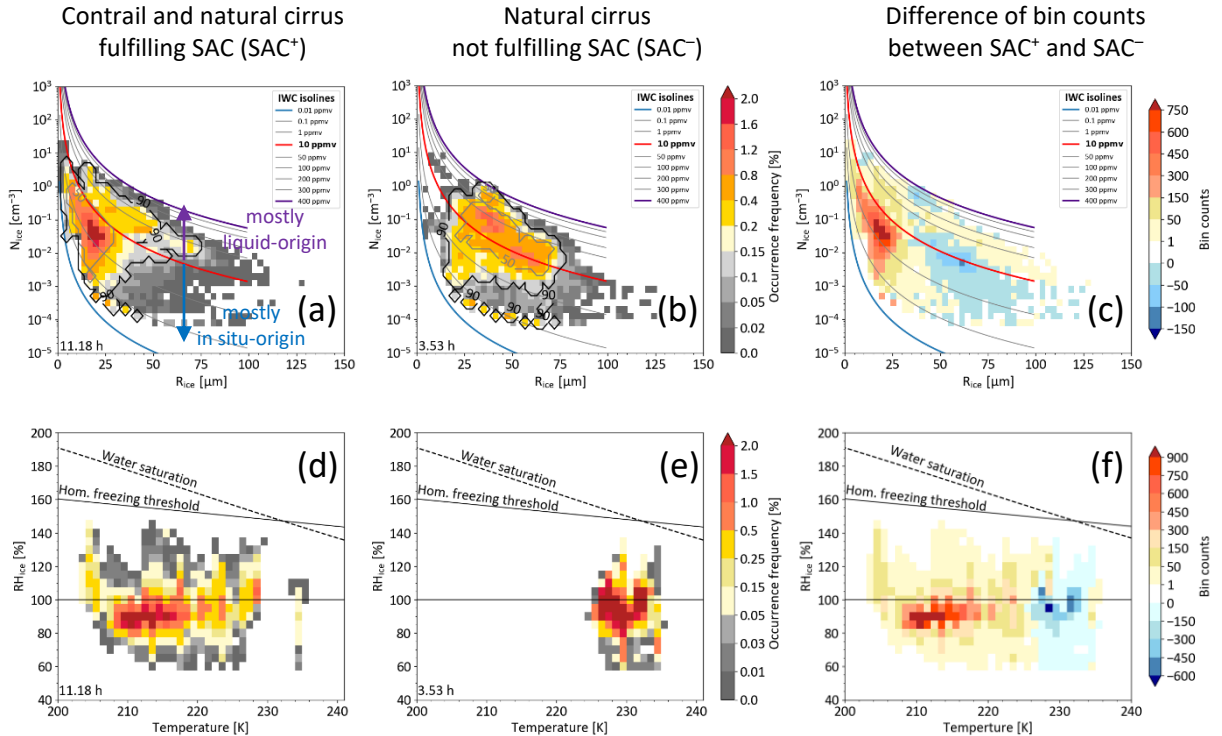
3.2.1.1 Microphysical properties in the cirrus fulfilling SAC and in natural cirrus

Figure 4a and b display the N_{ice} – R_{ice} relations for the SAC^+ and SAC^- datasets, respectively, with the occurrence frequency normalized to the total number of measurements in each dataset. Small ice crystals in higher concentrations are mainly found in the SAC^+ group. In the SAC^+ dataset, the median $N_{ice} = 0.04 \text{ cm}^{-3}$ doubles the median value of the SAC^- dataset. On the

320 contrary, the median R_{ice} of the SAC^+ group ($20.6 \mu m$) is only half of the value ($42.4 \mu m$) of its SAC^- counterpart. N_{ice} in the SAC^+ dataset reaches values as high as $20 cm^{-3}$ for R_{ice} smaller than $30 \mu m$, while N_{ice} in the SAC^- dataset is mostly below $1 cm^{-3}$ with most particles larger than $30 \mu m$. The highest occurrence frequencies in the SAC^+ and SAC^- datasets (enclosed by the 50th percentile contours) dwell on the lower and upper sides of the 10 ppmv IWC isoline, respectively.

Besides the fact that in the SAC^+ dataset both natural and contrail cirrus can be found, the SAC^- group contains only natural cirrus. The two groups largely correspond to cirrus formed from different mechanisms, namely in situ- and liquid-origin cirrus. Most in situ-origin ($IWC < 10 ppmv$) and some liquid-origin cirrus ($IWC > 10 ppmv$) are found in the SAC^+ group; conversely, most of the liquid-origin cirrus and a small part of the in situ-origin cirrus are in the SAC^- counterpart. Contrail cirrus belongs to the in situ-origin cirrus type, since it appears in the temperature range $T_{amb} < 235 K$, either without pre-existing cirrus (contrail cirrus) or superimposed on existing cirrus (embedded contrails). As embedded contrails, they could also appear as the liquid-origin cirrus.

330 The contrast between the SAC^+ and SAC^- groups is illustrated in Fig. 4c showing the differences between Fig. 4a and b. The reddish area indicates that ice crystals measured in the environments satisfying SAC are prone to contrail cirrus, whereas the bluish area, in contrast, shows ice crystals that are linked to natural cirrus.



335 **Figure 4.** Upper panels: similar to Fig. 3c, but for (a): the Schmidt-Appleman criterion (SAC) fulfilled dataset of contrail and natural cirrus (median: $N_{ice} = 0.04 cm^{-3}$ and $R_{ice} = 20.6 \mu m$); (b): the SAC unfulfilled dataset of natural cirrus (median: $N_{ice} = 0.018 cm^{-3}$ and $R_{ice} = 42.4 \mu m$); (c): the difference of data points between a and b in single N_{ice} – R_{ice} bins. Lower panels: similar to Fig. 3d, but for (d): the dataset of contrail or natural cirrus fulfilling SAC; (e): the natural cirrus not fulfilling the SAC; (f): the difference of data points between d and e in single RH_{ice} – T_{amb} bins.

340 3.2.1.2 RH_{ice} in the cirrus fulfilling SAC and in natural cirrus

The other pronounced differences between the SAC⁺ and SAC⁻ groups are the most frequently appearing RH_{ice} and the respective temperature ranges, as shown in the lower panel of Fig. 4. The highest occurrence frequencies of RH_{ice} in the SAC⁺ group concentrate at slight ice subsaturation at ~ 90% RH_{ice} in the T_{amb} range of 207–218 K. The slight ice-subsaturation feature is associated with younger contrails with high N_{ice} and small R_{ice}, as can be seen from Fig. S2b (see Supplement),
345 where the N_{ice}–R_{ice} relation is shown color-coded with RH_{ice} for the SAC⁺ group in the CA range (see Sect. 2.3.2). In the SAC⁻ dataset, the highest frequencies of RH_{ice} cluster around 100% at 10 K warmer temperatures and spread over the N_{ice}–R_{ice} parameter space (Fig. S2c). The warm temperature range, which is already shown in Fig. 2, reflects the fact that colder temperatures are needed to fulfil SAC because the water saturation pressure at warmer temperatures is almost always so high that the amount of water in the ambient air together with the additional water from aircraft exhaust is insufficient to reach
350 supersaturation with respect to water to form droplets.

In spite of the clear differences in ice particle properties and ambient RH_{ice} conditions resulted from applying SAC (Fig. 4f), ambiguities remain to characterise contrail cirrus and distinguish them from natural cirrus, because the natural cirrus of in situ-origin that have formed at rather low temperatures can show as well the characteristics of medium N_{ice} (0.1 cm⁻³), low IWC and small R_{ice}, and would thus be misclassified as contrail cirrus. Additionally, even high N_{ice} accompanied by small R_{ice}
355 can appear in natural cirrus as a result of in situ homogeneously freezing in high updrafts (Krämer et al., 2016).

3.2.2 Cirrus fulfilling SAC inside and outside the cruising altitude (CA) range

Here, the SAC⁺ dataset shown in Fig. 4a and d is split into one group inside the most frequent cruising altitude (CA) range and the other one outside the CA range using the CA pressure boundaries defined in Sect. 2.3.2. The ice cloud properties and RH_{ice} occurrence frequencies related to ambient temperature inside and outside the CA range are presented and discussed below.

360 3.2.2.1 Microphysical properties inside and outside the cruising altitude range

The N_{ice}–R_{ice} relation of the cirrus fulfilling the SAC and detected inside the CA range is shown in Fig. 5a, while those outside the CA range are depicted in Fig. 5c. Comparing the N_{ice}–R_{ice} relation showing all SAC⁺ cirrus (Fig. 4a) to those inside and outside the CA range, it becomes visible that the entire group of liquid-origin cirrus (R_{ice} > 30 μm and IWC > 10 ppmv) and a part of the in situ-origin cirrus (R_{ice} < 30 μm and IWC < 10 ppmv) occur outside the CA range, *i.e.*, the cirrus outside the CA
365 range represent a mixture of contrail cirrus, in situ-origin cirrus as well as liquid-origin cirrus, later referred to as cirrus mixture. Inside the CA range, almost only in situ-origin cirrus are present. The mean R_{ice} and N_{ice} of cirrus particles inside the CA range (Fig. 5a) are approximately 17 μm and 0.21 cm⁻³, corresponding to previous field observations of pure contrail cirrus older than 30 minutes (Schröder et al., 2000; Voigt et al., 2017; Schumann et al., 2017; Chauvigné et al., 2018).

The classification that the cirrus fulfilling SAC and inside the CA range are pure contrail cirrus is confirmed by the validated
370 contrail cirrus, which fulfil SAC and are identified by applying the aircraft plume detection algorithm (Mahnke et al., 2022) described in Sect. 2.3.3. Since the aerosol and NO_y measurements for both flights on 22 March 2014 were missing and that

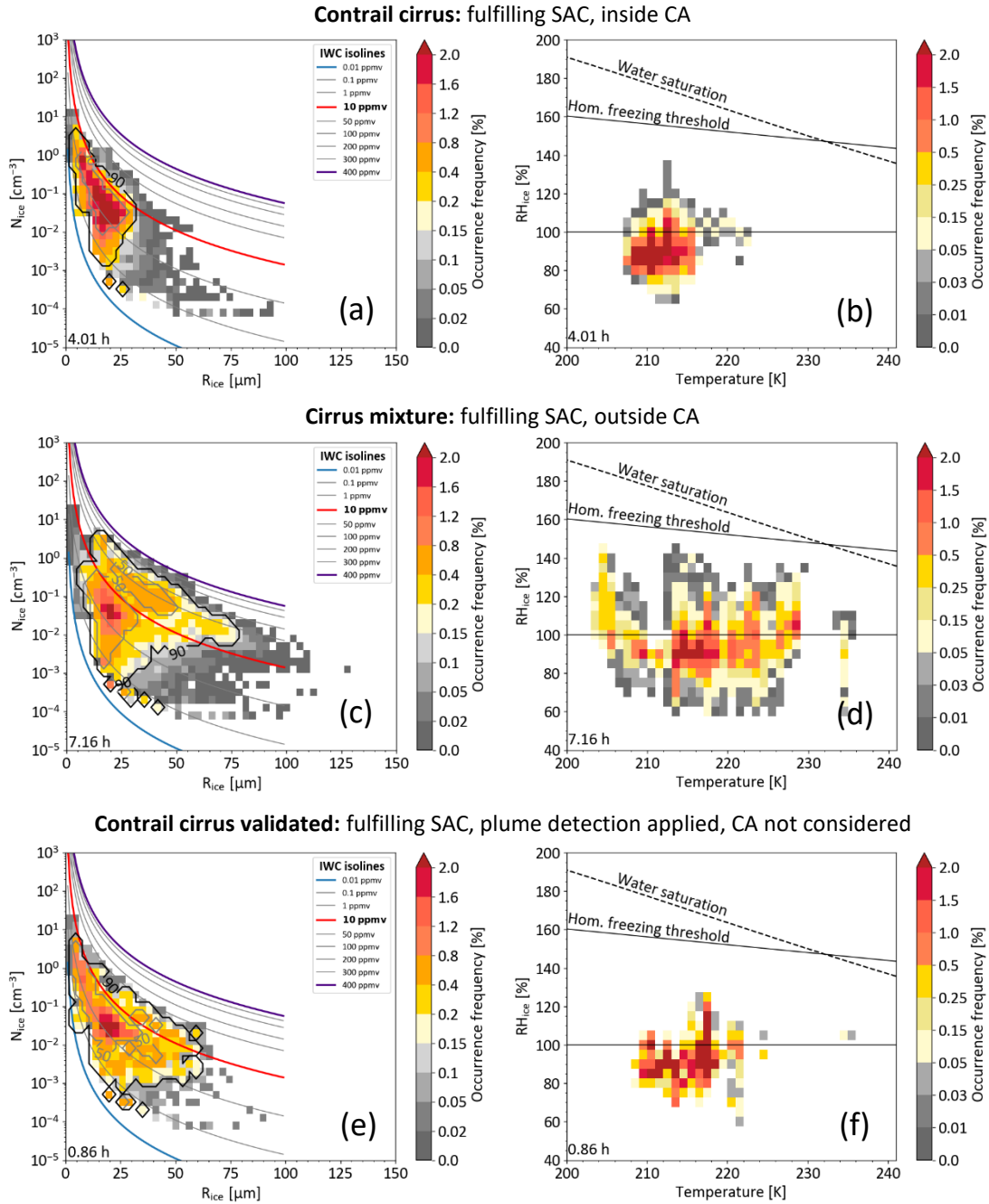
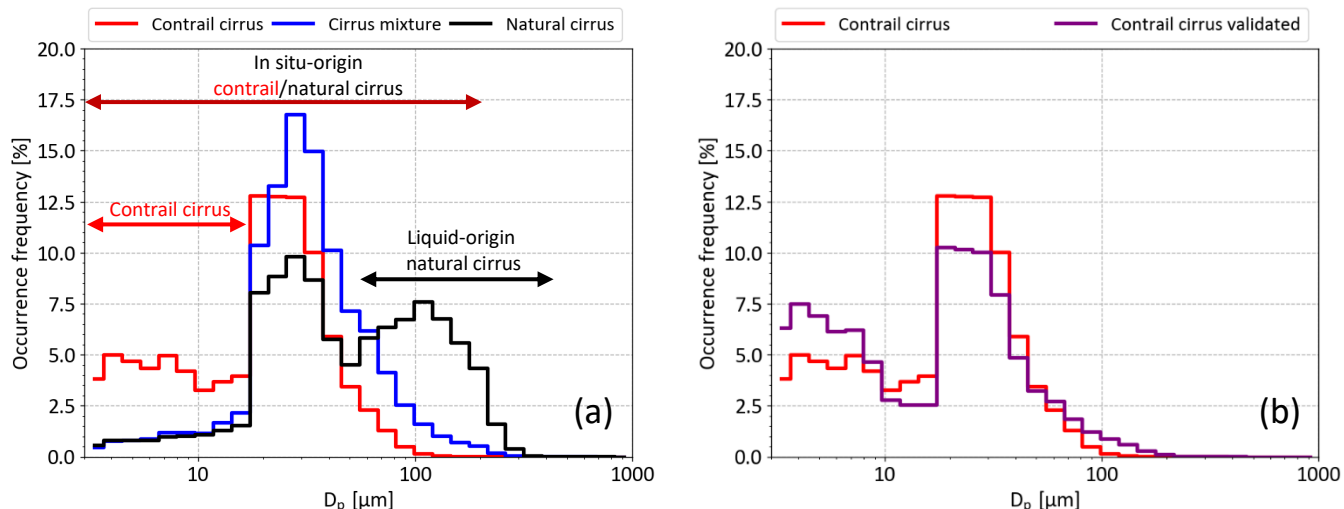


Figure 5. N_{ice} – R_{ice} (left) and RH_{ice} – T_{amb} (right) relations color-coded by normalised occurrence frequency, similar to those in Fig. 4. Top: the contrail cirrus fulfilling the Schmidt-Appleman criterion (SAC) and found inside the cruising altitude range (CA, ambient pressure 200–245 hPa) (median: $N_{ice} = 0.045 \text{ cm}^{-3}$ and $R_{ice} = 16.6 \text{ }\mu m$). Middle: the cirrus mixture fulfilling SAC and outside the CA range (in situ- and liquid-origin cirrus) (median: $N_{ice} = 0.038 \text{ cm}^{-3}$ and $R_{ice} = 24.1 \text{ }\mu m$). Bottom: contrail cirrus with plume detection applied and fulfilling the SAC (median: $N_{ice} = 0.027 \text{ cm}^{-3}$ and $R_{ice} = 21.7 \text{ }\mu m$), but the CA range is not considered here.



380 **Figure 6.** (a): Normalised occurrence frequency of ice particle sizes in diameter (D_p , unit: μm) in the contrail cirrus (red), cirrus mixture
 (contrail cirrus, in situ- and liquid-origin natural cirrus, blue), and natural cirrus (black). The ice particle size ranges for contrail cirrus, in
 situ-origin contrail or natural cirrus, and liquid-origin cirrus are marked by the arrows. (b): Similar to (a) but for contrail cirrus (red) and
 contrail cirrus satisfying the Schmidt-Appleman criterion (SAC) and validated with the aircraft exhaust plume detection method (purple).
 Note that D_p stands for optical equivalent diameter for NIXE-CAS-DPOL in the size range of 3–17 μm and area equivalent diameter for
 NIXE-CIPg in the sizes greater than 17 μm .
 385

aircraft plumes detected at $T_{\text{amb}} > 235$ K are screened out, the valid sampling time encountered aircraft exhaust plumes is
 approximately 0.9 hr, around 3200 cloud samples at 1Hz sampling frequency, among which 1270 cloud samples are located
 in the CA range. As adding the CA constraint to the SAC fulfilled plume dataset does not improve the validation significantly
 (See Sect. S4 in the Supplement for detailed analysis), the following discussion is based on the plume dataset with only the
 390 SAC applied.

The $N_{\text{ice}}\text{--}R_{\text{ice}}$ relation for the validated contrail cirrus is displayed in Fig. 5e. The shape of the overall $N_{\text{ice}}\text{--}R_{\text{ice}}$ occurrence
 frequency distribution for the validated contrail cirrus shows similarity to the pure contrail cirrus differentiated by combining
 SAC and the CA range (Fig. 5a), especially when looking at the particle population that contains 50% of the most frequently
 appearing ice crystals. The median R_{ice} and N_{ice} of the pure contrail cirrus are also close to those of the validated cirrus. In
 395 conclusion, combining SAC and the CA range has effectively exposed the differences in the microphysical properties of pure
 contrail cirrus (SAC^+ , inside the CA range, Fig. 5a), a cirrus mixture (SAC^+ , outside the CA range, Fig. 5c) and mostly liquid-
 origin natural cirrus (SAC^- , outside the CA range, Fig. 4b).

Besides, we also inspected the frequency distributions of ice particle sizes in diameter, which are not integrated like mass mean
 radius and will give further insights into the differences among the cirrus categories and, in addition, confirm the differentiation
 400 using the SAC-CA method.

Figure 6a shows the normalised occurrence frequencies of ice particle sizes in the contrail cirrus (in situ-origin), cirrus mixture
 (contrail cirrus, in situ- and liquid-origin natural cirrus) and mostly liquid-origin natural cirrus. Three size modes of ice particle
 sizes can be identified from the frequency distributions of the contrail cirrus and natural cirrus: ice particles in the first size

mode — $D_p = 3\text{--}17\text{ }\mu\text{m}$ (marked by the short red arrow) — appear more frequently inside the CA range and are attributed to pure contrail cirrus; The next size mode — $D_p = 3\text{--}200\text{ }\mu\text{m}$ (the long red arrow) — is present in contrail cirrus as well as in natural cirrus and is attributed to aged contrails or in situ-origin natural cirrus; the mode $D_p = 50\text{--}400\text{ }\mu\text{m}$ (the black arrow) originates from liquid-origin cirrus. The maximum sizes represent the largest ice particle size of the particle population including 90% data. Large ice crystals up to about $200\text{--}300\text{ }\mu\text{m}$ do appear in contrail cirrus but with a low frequency (see the blue curve in Fig. 6a and also Kübbeler et al., 2011; Voigt et al., 2010). Also, note that $20\text{ }\mu\text{m}$ marks the instrument switches from NIXE-CAS-DPOL to NIXE-CIPg. This might cause the jump of occurrence frequencies instead of a smooth transition. The histograms in Fig. 6a show that the contrail (red line) and liquid-origin natural (black line) cirrus are most probably distinguishable in the small ice particle diameter range ($D_p < 17\text{ }\mu\text{m}$) and the larger size range ($D_p > 80\text{ }\mu\text{m}$). Ice crystals between $D_p = 17\text{--}45\text{ }\mu\text{m}$ occur frequently in the contrail cirrus, but also in the natural cirrus, which makes it difficult to discriminate between the contrail and natural cirrus in this size range. The signature of a larger number of small ice crystals in natural cirrus occurs in the early phase of homogeneous ice nucleation in faster updraughts. However, such events are transient in time and space, and are, therefore, not often found in in situ measurements (Krämer et al., 2020). The contrail cirrus considered here does not contain such homogeneous freezing events. Therefore, ice crystals in the diameter range $D_p = 3\text{--}17\text{ }\mu\text{m}$ with relatively high occurrence frequencies and the large particles of maximum size of about $200\text{ }\mu\text{m}$ can be attributed to contrail cirrus, as already noted above. On the contrary, the natural cirrus has the second highest frequency peak in the ice crystals larger than $54\text{ }\mu\text{m}$ with the maximum diameter being about $400\text{ }\mu\text{m}$. This means that the observed contrail cirrus were formed in situ with the special feature of frequently appearing small ice crystals; the natural cirrus, however, as introduced before, is a mixture of in situ-origin and liquid-origin cirrus. It is to note here that adding an extra constraint of the CA range to the SAC⁺ group has greatly minimised the interference of the natural cirrus as well as possibly undistinguishable, deeply aged contrail cirrus of much larger sizes.

The cirrus mixture is interpreted above as a mixture of aged contrail cirrus, mainly in situ-origin cirrus with a small portion of middle-sized liquid-origin cirrus. This is confirmed by the frequency distribution of ice particle sizes shown in Fig. 6a (blue line), where the majority (80% of the total frequencies) of particle diameters are between 17 and $66\text{ }\mu\text{m}$ and the maximum size is near $300\text{ }\mu\text{m}$. From this analysis, it is impossible to judge whether the in situ-origin cirrus are aged contrails, which show the same properties as natural cirrus, or whether these cirrus have formed naturally.

Figure 6b shows that the occurrence frequency distribution of ice particle sizes in the contrail cirrus identified using the SAC-CA combination is very similar to that of the validated contrail cirrus aided by the plume detection scheme. In the reference case of the plume-marked contrail cirrus, there are even more smaller ice particles than in the SAC-CA determined contrail cirrus. Furthermore, the large ice particles occur with very low frequencies not only in the plume-marked contrail cirrus but also in the contrail cirrus constrained by SAC and the CA range. This adds confidence in the discrimination between contrail cirrus and natural cirrus with the SAC-CA combination.

3.2.2.2 RH_{ice} inside and outside the cruising altitude range

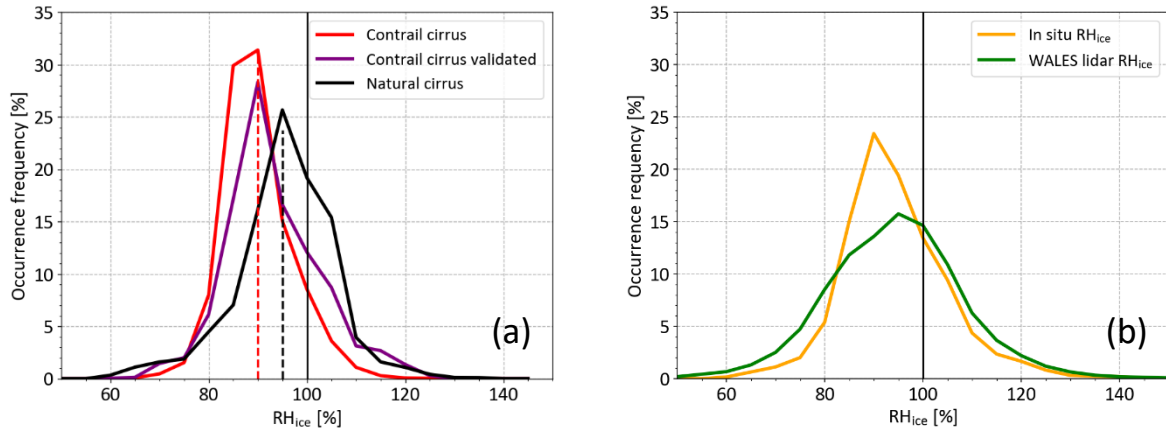
The $RH_{ice}-T_{amb}$ distribution for the contrail cirrus (SAC^+ , inside the CA range) is shown in Fig. 5b, while Fig. 5d depicts that for the cirrus mixture (SAC^+ , outside the CA range). In comparison to Fig. 4e, where the frequencies of RH_{ice} in the natural cirrus (SAC^-) centre around 100% at temperatures above 225 K (also reported in regional and global research flight measurements by Krämer et al. (2020), Patnaude et al. (2021), Diao et al. (2014); (2017) and RH_{ice} observations on board passenger aircraft by Spichtinger et al. (2004), the RH_{ice} inside the contrail cirrus (Fig. 5b) distributes most frequently around 90% and appears almost exclusively in the temperature range $T_{amb} = 207-218$ K. As mentioned in Sect. 3.2.1, this subsaturation feature is associated with high N_{ice} and small R_{ice} inside the CA range (Fig. 5a), namely the contrail cirrus, as discussed in previous subsections and shown in the $N_{ice}-R_{ice}$ relations color-coded with RH_{ice} in Fig. S2 (see Supplement). Compared to the RH_{ice} distribution in the contrail cirrus (Fig. 5b) and natural cirrus (Fig. 4e), the RH_{ice} frequencies in the cirrus mixture (in Fig. 5d) are more broadly distributed around 100% RH_{ice} between 204 and 229 K, yet with slightly higher frequencies between 80 and 100% at $T_{amb} = 207-218$ K, similar to the contrail cirrus. The high RH_{ice} values up to 140% in the cirrus mixture are closely related to the in situ-origin cirrus ($N_{ice} < 0.1 \text{ cm}^{-3}$ and $R_{ice} < 30 \text{ }\mu\text{m}$) and liquid-origin cirrus ($IWC > 10 \text{ ppmv}$, $R_{ice} > 50 \text{ }\mu\text{m}$), as seen from Fig. S2d.

Figure 5f shows that RH_{ice} in the validated contrail cirrus falls mostly below ice saturation in the temperature range of 208–228 K, consistent with the ice-subsaturation feature in the pure contrail cirrus (Fig. 5b). We consider the agreement as verification of the method for separating contrail cirrus from natural cirrus by using only SAC and the CA range.

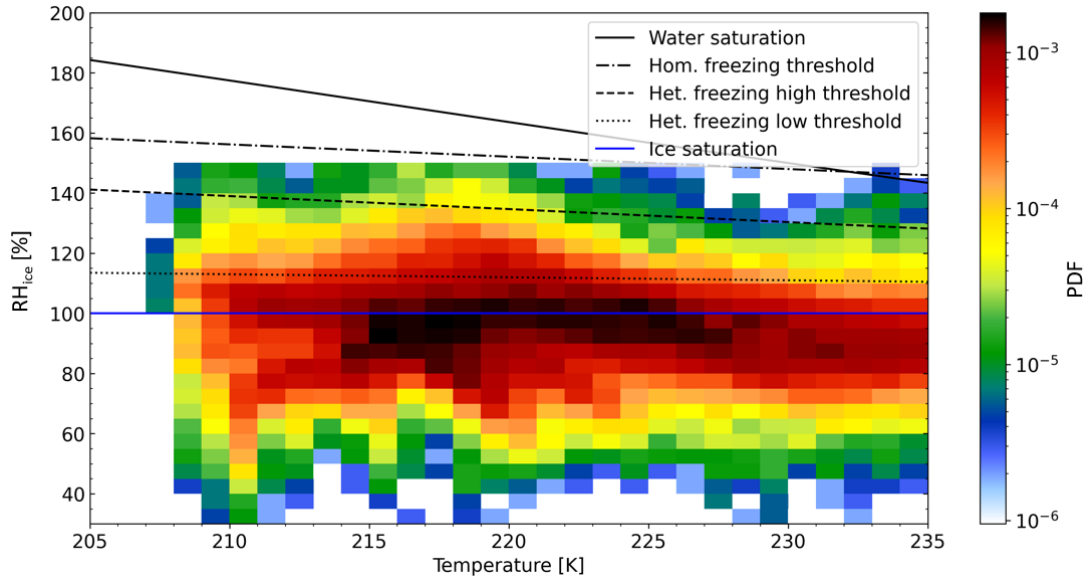
3.3 In-cloud ice sub- and supersaturation — comparisons and causes

In Fig. 7a, we present the RH_{ice} occurrence frequencies of the different cirrus types distinguished using the criteria of SAC, CA and plume detection: the contrail cirrus, validated contrail cirrus (identified using the plume detection method) and natural cirrus. RH_{ice} in the contrail and the validated contrail cirrus peaks at 90% RH_{ice} , *i.e.*, in slight ice subsaturation, with much higher occurrence frequency than at 100% RH_{ice} . Furthermore, the RH_{ice} distribution in the contrail cirrus tilts to the left — lower ice subsaturation (80% RH_{ice}), while the distribution of RH_{ice} in the natural cirrus has a heavier weight in the right part of the peak — more towards ice supersaturation (110%).

The slight subsaturations observed here seems to be doubtful, although previous instrumental intercomparisons have suggested that there is no non-negligible bias in the RH_{ice} measurements (see Sect. 2.1). However, the possibility of a small bias in the in situ RH_{ice} dataset due to a low bias in the T_{amb} measurement was brought up in Schumann (2021; See page 108). Later in this section, the effect of a possible low T_{amb} bias will be discussed in relation to the observation of ice subsaturation contrail cirrus. But first, the in-cloud RH_{ice} occurrence frequency distribution from the WALES lidar observations (see Sect. 2.1) is plotted in Fig. 7b in comparison to the in situ RH_{ice} of all cirrus. The RH_{ice} distribution of all in situ measured cirrus (the orange curve) peaks at 90% RH_{ice} with an occurrence frequency of $\sim 22\%$, nearly overlapped with the distribution of the lidar RH_{ice} shown in green, which is broader with a blunt peak around 95% RH_{ice} ($\sim 15\%$ of occurrence frequency). The lidar RH_{ice} of mixed contrail and natural cirrus spans from approximately 80–110% at the full width half maximum of the peak, the same RH_{ice} range observed in most in situ measurements. Despite the different T_{amb} sources used for the in situ RH_{ice} (from BAHAMAS)



475 **Figure 7.** (a): Normalised RH_{ice} occurrence frequency distributions in 5% RH_{ice} bin width for the contrail cirrus identified using the combination of the Schmidt-Appleman criterion (SAC) and the cruising altitude range (CA) (red), contrail cirrus validated by the plume detection algorithm (purple) and natural cirrus not fulfilling SAC and located outside the CA range (black). The most frequently occurring RH_{ice} in the contrail cirrus and natural cirrus are marked by the red and black dashed lines, respectively. (b): Normalised RH_{ice} occurrence frequency distributions for all cirrus measured in situ (orange) and by the lidar WALES (green).



480 **Figure 8.** Probability distribution of in-cloud RH_{ice} measured by the lidar WALES below 235 K in dependence on ECMWF model temperature. Only the cloud particles producing a back-scattering ratio greater than 3 and a depolarisation ratio greater than 20% are included in the plot. The water saturation (Murphy and Koop, 2005), homogeneous freezing threshold (Koop et al., 2000), and heterogeneous freezing high (mineral dust as ice nucleating particles) and low (coated soot) thresholds (Krämer et al., 2016) are added in the figure. Ice saturation is also marked by the blue horizontal line.

485 and lidar RH_{ice} (from ECMWF) calculations, the RH_{ice} distributions related to temperature of in situ (see Fig. 3d) and remote sensing measurements (see Fig. 8) in the same environment exhibit a consistent view of RH_{ice} occurrence frequencies in the cirrus clouds in Central Europe and the Northeast Atlantic flight corridor in Spring 2014. The subsaturation feature of cirrus is also evident in the temperature dependence of the lidar RH_{ice} at cold temperatures between ~ 215 – 220 K, while at warmer temperatures above 220 K, RH_{ice} centres at around 100% . The good agreement between the independent in situ and lidar RH_{ice} measurements gives confidence in the assignment of the slight ice-subsaturation feature to contrail cirrus.

490 However, because of the strong dependence of RH_{ice} on the T_{amb} , the above-mentioned effect of a negative temperature bias on the RH_{ice} distribution is tested because lower temperatures enhance RH_{ice} . The change in RH_{ice} frequency distribution in all cirrus clouds by lowering the ambient temperature by 0.5 K is shown in Fig. S3 (see Supplement). The peak of the RH_{ice} frequency distribution shifts from 90% to 95% , so the slight ice-subsaturation feature is still visible in the contrail cirrus above
495 Central Europe and the Northeast Atlantic region in Spring 2014.

Since finding contrail cirrus in an ice-subsaturated environment may seem surprising, we discuss possible reasons for this in the following. During the campaign phase in Spring 2014, the background atmosphere in the investigated region was relatively calm with slow vertical velocities mostly below 0.2 m/s in frontal systems and warm conveyor belts. Why contrail cirrus were sampled in slight ice-subsaturation can be assumed from two perspectives:

- 500 1. Contrails could have formed in slight ice-supersaturation in pre-existing thin/subvisible cirrus, which have been formed heterogeneously and of which the ice particles have grown to large sizes (Kübbeler et al., 2011). Marjani et al. (2022) have revealed from satellite retrievals that the perturbation of aircraft on cirrus ice number concentrations is located 300 – 540 metres beneath the flight tracks, right where the primary aircraft vortex descends after formation. The temperature increase accompanying this descent causes RH_{ice} to decrease to ice-subsaturation accompanied,
505 which was observed for instance by Gayet et al. (2012; Fig. 3h). In such cases, the occurring cirrus would be contrail cirrus embedded in already existing, possibly subvisible natural cirrus.
2. Contrails could also have formed in slightly ice-subsaturated to slightly supersaturated environments where natural cirrus could not emerge because the threshold humidity for heterogeneous freezing is not reached. But water vapour in the environment together with that emitted from aircraft is sufficient to surpass water saturation and form a contrail
510 in the hot and moist aircraft exhaust. Mixing of the ambient air together with the descent to lower altitudes as described in (1) would also place the contrail cirrus in a subsaturated environment. The question here is if the ice crystals can grow to the observed sizes of maximum ~ 200 μm during their time in supersaturation. However, this would be the classic case of a blue sky without any cirrus cloud, which turns into a grey sky covered with contrail cirrus in the presence of air traffic.

515 The next obvious question regarding how long the contrail cirrus can persist in a slightly ice-subsaturated environment will be discussed in Sect. 4.

3.4 Survey of cirrus and contrail cirrus characteristics

Table 1. Percentiles of ice number concentration N_{ice} , mass mean radius R_{ice} , ice water content IWC, relative humidity with respect to ice RH_{ice} and Extinction coefficient Ext in the contrail cirrus, the contrail cirrus validated with the aircraft plume detection algorithm, the cirrus mixture and the natural cirrus over Central Europe and the Northeast Atlantic region in Spring 2014.

Cirrus categories		Contrail cirrus	Contrail cirrus	Cirrus mixture	Natural cirrus
SAC ¹		+	+	+	–
CA ²		+	+	–	–
Plume detection ³		NA	A	NA	NA
Temperature range		207–218 K	208–217 K	< 207 K, 218–225 K	225–235 K
Data points (1 Hz)		14454	1270	25791	12691
Phase relaxation time ⁴ (τ_{ph})		~ 30 min	~31 min	~ 27 min	~ 35 min
N_{ice} [cm^{-3}] ($D_p > 3 \mu m$)	10. perc	0.006	0.014	0.003	0.001
	25. perc	0.018	0.024	0.011	0.005
	50. perc	0.045	0.041	0.038	0.018
	75. perc	0.135	0.131	0.112	0.069
	90. perc	0.454	0.642	0.309	0.170
R_{ice} [μm]	10. perc	7.8	6.7	14.8	24.5
	25. perc	12.3	11.6	18.3	32.4
	50. perc	16.6	17.8	24.1	42.4
	75. perc	20.9	21.5	37.8	55.2
	90. perc	24.9	24.6	52.7	65.3
IWC [ppmv] (IWC ⁵ [mg/m^3])	10. perc	0.5 (0.1)	0.8 (0.2)	0.5 (0.1)	1.0 (0.3)
	25. perc	1.4 (0.3)	2.1 (0.5)	2.4 (0.6)	6.3 (1.8)
	50. perc	3.5 (0.8)	4.4 (1.0)	8.3 (2.1)	21.7 (6.1)
	75. perc	6.4 (1.5)	6.6 (1.6)	44.7 (13.1)	58.1 (16.7)
	90. perc	10.9 (2.6)	10.0 (2.4)	95.4 (28.8)	105.0 (16.7)
RH_{ice} [%]	10. perc	82.5	80.5	83.4	83.1
	25. perc	85.5	85.7	88.9	90.5
	50. perc	88.8	88.9	94.3	95.9
	75. perc	93.4	92.7	102.9	101.8
	90. perc	99.6	98.9	112.1	106.2
Ext^6 [km^{-1}]	10. perc	0.008	0.015	0.006	0.0109
	25. perc	0.023	0.036	0.031	0.045
	50. perc	0.056	0.061	0.096	0.137
	75. perc	0.109	0.102	0.351	0.414
	90. perc	0.184	0.191	0.888	0.841

¹SAC: the Schmidt-Appleman criterion, “+” fulfilling SAC, “–” not fulfilling SAC.

²CA: the cruising altitude range, “+” inside CA, “–” outside CA.

³Plume detection: the plume detection algorithm, “A” applied, “NA” not applied.

⁴Phase relaxation time: the time for in-cloud air in ice-subsaturation to reach saturation under quasi-steady conditions (Korolev and Mazin, 2003), *i.e.* with no vertical movement of the air parcels.

⁵IWC [mg/m^3]: ice water content in mg/m^3 is converted from the IWC in ppmv using H_2O molar mass, ambient pressure and temperature.

⁶Ext: the extinction coefficient. It’s calculated after the equation (3) in Gayet et al. (2004) with IWC in g/m^3 ; See the text for details.

The 10th, 25th, 50th, 75th and 90th percentiles of the different characteristics of the cirrus types, detected over Central Europe in Spring 2014 and separated by the combined analysis of SAC, CA and the plume detection scheme (Section 2.3), are summarised in Table 1. The median N_{ice} , R_{ice} , IWC and RH_{ice} in the contrail cirrus constrained by SAC and the CA range as well as those contrail cirrus identified using the aircraft exhaust detection method are correspondent, giving confidence in the new, statistically based contrail–cirrus separation method.

The parameters determining the probable origin, optical property and evolution state of the clouds are the median IWC (Sect. 1), extinction coefficient (Ext) and RH_{ice} . Ext is calculated from the empirical formulation in Gayet et al. (2004): $D_{eff} = A \times IWC / Ext$, where the effective diameter D_{eff} is in μm , IWC is in g/m^3 (calculated from IWC in ppmv using H_2O molar mass, ambient pressure and temperature) and $A = 3000 \text{ mm}^3/g$. The D_{eff} is converted from the mass mean radius R_{ice} , assuming a ratio of 0.7 ± 0.3 between R_{ice} and the effective radius R_{eff} of ice particles in contrails and contrail cirrus based on Schumann et al. (2011). The uncertainty of the Ext is approximately $\pm 43\%$. For contrail cirrus, found in the temperature range 207–218 K, these are $IWC = 3.5 \text{ ppmv}$, $Ext = \sim 0.056 \text{ km}^{-1}$ and $RH_{ice} = 88.8\%$, thus classifying them as in situ-origin, optically thin, sublimating cirrus clouds (Fig. 11, left panel). The warm, natural cirrus (temperature range 225–235 K) are mostly liquid-origin, thick, persisting cirrus (Fig. 11, right panel) exhibiting a higher median IWC (21.7 ppmv), a larger $Ext = \sim 0.137 \text{ km}^{-1}$ and $RH_{ice} = 95.9\%$ close to saturation. The cirrus mixture, with contrails embedded within in situ-and liquid-origin cirrus (Fig. 11, middle panel), are in the intermediate temperature range of 218 to 225 K. Their median properties are $IWC = 8.3 \text{ ppmv}$, $Ext = \sim 0.096 \text{ km}^{-1}$ and $RH_{ice} = 94.3\%$; however, no clear assignment is made here due to their mixed nature. The slightly subsaturated contrails observed under the conditions (R_{ice} , N_{ice} , RH_{ice} , temperature range shown in Table 1) would need ~ 30 min to relax to ice saturation after their descent is completed (assuming no vertical motion and changes in the ice particle size negligible) (Korolev and Mazin, 2003), while it would take slightly longer for the natural cirrus to reach saturation.

4 Persistent cirrus in slight ice-subsaturation – potential influence on aviation’s climate impact

The slight ice-subsaturation feature of the contrail cirrus observed over Central Europe in Spring 2014 agrees with the occurrence of contrails in ice subsaturated atmosphere that was observed during the CONCERT campaign (Kübbeler et al., 2011; Voigt et al., 2010; Gayet et al., 2012), although contrail cirrus crystals sampled during ML-CIRRUS were much older (Schumann et al., 2017; Voigt et al., 2017) than those young contrails at the age of a few minutes detected during the CONCERT campaign (Voigt et al., 2010; Chauvigné et al., 2018). A comprehensive compilation of contrails and contrail cirrus measurements from a series of research aircraft campaigns confirmed that the occurrence in slight subsaturation with respect to ice is a pronounced characteristic of contrail cirrus (Schumann et al., 2017). Furthermore, Petzold et al. (2017) reported the observation of contrail cirrus in slight ice subsaturation in the North Atlantic flight corridor using RH_{ice} measurements aboard the passenger aircraft in the IAGOS research infrastructure. Concluding, contrail cirrus occurrence in slight ice subsaturation is not an uncommon feature.

Whether the contrail cirrus existing in slight ice subsaturation might affect the radiative forcing is connected to the lifetime of ice crystals in such environment. Therefore, we investigated the lifetime of cirrus ice particles of the size and concentration identified for contrail cirrus in slight ice subsaturation using the SAC-CA combination. A scenario of cirrus cloud particles
555 formed at $T_{\text{amb}} < 210$ K was simulated using the detailed microphysical box model MAID (Model for Aerosol and Ice Dynamics) (Bunz et al., 2008; Rolf et al., 2012; Krämer et al., 2016). The simulation was initialised with a water amount of 90% RH_{ice} (T_{amb}) and an ice-nucleating particle concentration of 0.1 cm^{-3} . The adiabatic cooling or warming rate at vertical wind speeds of 0.1 m/s was added to present the constant updraughts or downdraughts in the atmosphere. Ice crystal sublimation and sedimentation processes were not considered in the simulation. The formation and evolution of cirrus particles
560 in the simulated scenario are plotted in Fig. 9. As contrail cirrus formation process is not implemented in the model, the cooling phase of the simulated scenario in Fig. 9 is to produce cirrus particles that have the similar properties ($N_{\text{ice}} = 0.2 \text{ cm}^{-3}$ and $R_{\text{ice}} = 17 \text{ }\mu\text{m}$, Fig. 5a, within the 50% contour) to the contrail cirrus separated by the combined SAC-CA method. Driven by the vortex dynamics, the distribution of the vertical velocity in the wake of aircraft is distorted towards downdrafts, different from natural cirrus. The warming phase in Fig. 9 simulates the descending of contrails to several hundred meters below flight altitude, after their formation in primary aircraft vortex; See Sect. 3.3. As the warming procedure reduces RH_{ice} to below ice
565 altitude, the warming procedure reduces RH_{ice} to below ice

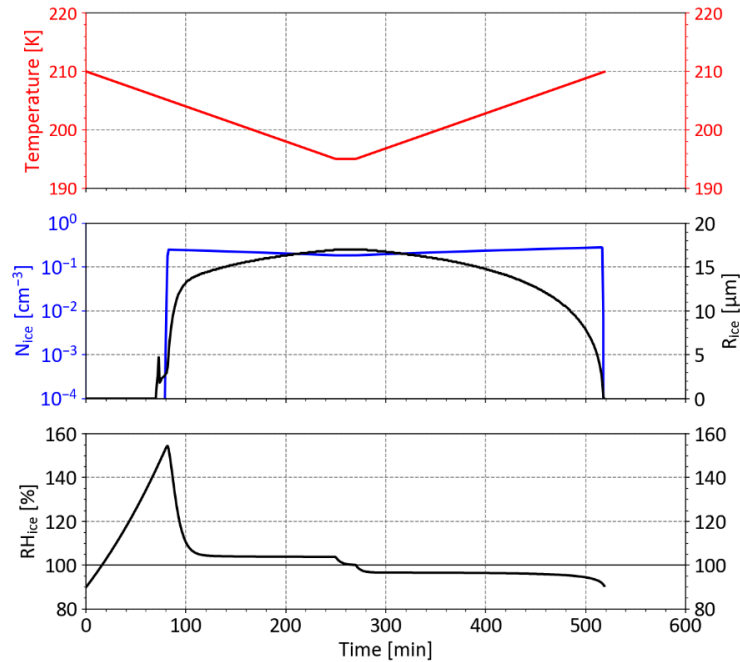


Figure 9. Simulated evolution of cirrus cloud particles initialised at 210 K and 90% RH_{ice} in dependence on the simulation time in minutes. Top: temperature of air parcels (unit: K). Middle: ice particle number concentration N_{ice} (cm^{-3} , blue) and mass radius mean R_{ice} (μm , black) of cirrus crystals. Bottom: relative humidity with respect to ice RH_{ice} (%).

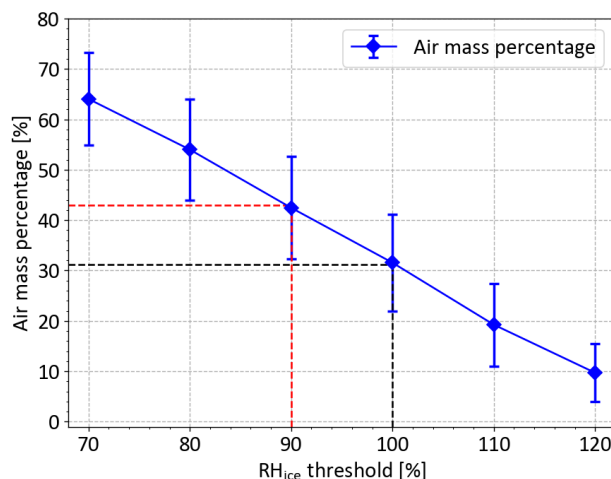


Figure 10. Percentage of air masses in dependence on RH_{ice} thresholds in the upper troposphere, averaged over the North Atlantic (65° – 5° W) and Europe (5° W– 30° E) regions for the MOZAIC period from 1995 to 2010. The percentages of air masses above 90% and 100% RH_{ice} thresholds are labelled with the red and black dashed lines, respectively.

saturation, cirrus ice particles of similar properties to the observed contrail cirrus gradually diminish, which takes approximately 4 h for the ice particles to sublimate until RH_{ice} declines to below 80%. This implies that contrail cirrus existing in a slightly ice- subsaturated environment could survive for a long-time scale, during which they might also alter the Earth’s radiation budget, similar to the persistent contrails formed in ISSRs.

Whether slightly ice-subsaturated regions are relevant for the influence of contrail cirrus on climate depends on the frequency of the occurrence of such regions. For this reason, we assessed the changes in air masses for a further potential radiative impact of contrail cirrus when lowering the threshold of contrail persistence in RH_{ice} from 100% to 90%. Figure 10 summarises the air mass percentages under different RH_{ice} thresholds averaged over the North Atlantic and Europe for the IAGOS-MOZAIC observational period from 1995 to 2010 (see Petzold et al., 2020 for details). The air mass percentage of $RH_{ice} \geq 90\%$ for the Europe and North Atlantic flight corridor is approximately 43%, increased by more than 10% in comparison to the air mass percentage of $RH_{ice} \geq 100\%$. Whether this finding might lead to a larger impact of aviation on the climate is unclear, particularly when the recent results on the relevance of strong warming contrails, the so-called big hits (Teoh et al., 2020b; Gierens et al., 2020) are considered.

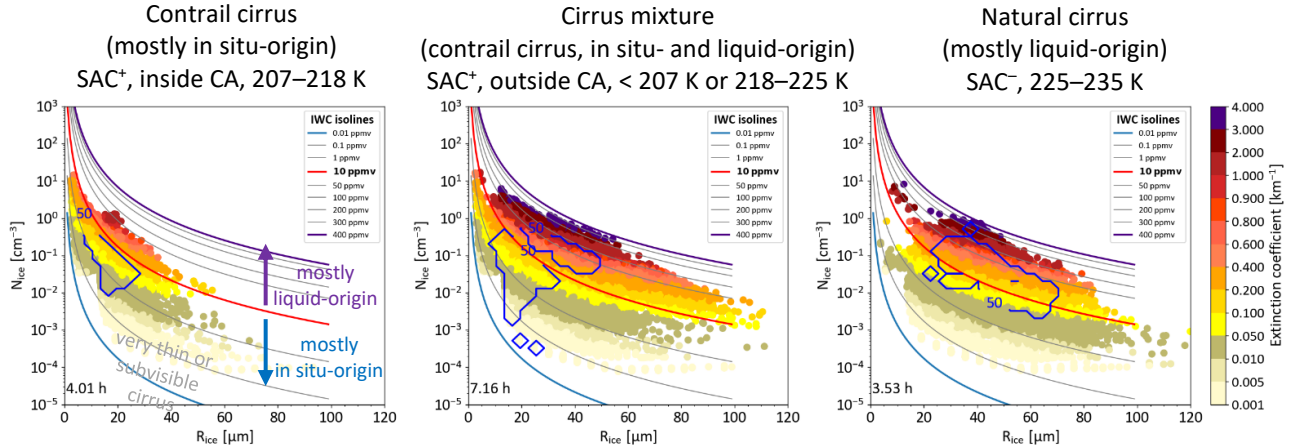
The climate impact of aviation-induced cirrus clouds by today’s knowledge is predominantly linked to contrail cirrus in ISSRs. So is the current recommendation for diverting the aircraft to avoid the formation of contrails with strong radiative forcing potential (Teoh et al., 2020a; 2020b). It is unclear how the existence of contrail cirrus in slightly ice-subsaturated regions could influence the assessment of the climate impact of contrails and contrail cirrus. However, as we have shown in our analysis, contrail cirrus do survive several hours in such slight ice-subsaturation (90% RH_{ice}), and there might be a non-negligible increase in contrail cirrus coverage if considering the existence of contrail cirrus in $RH_{ice} \geq 90\%$. Thus, we recommend

considering the slightly ice-subsaturated regions for the benefit of safe contrail avoidance during air traffic management and a reliable estimation of the radiative forcing of aviation-induced cloudiness.

595 5 Summary

Fresh contrails can be easily identified owing to their brightness and linear shape. Apart from that, contrail cirrus, especially those aged into thin cirrus layer, are difficult to be separated from natural cirrus to tackle aviation-induced climate impact. In this work, a new approach to filter out contrail cirrus from natural cirrus is developed: we combined the Schmidt-Appleman criterion (SAC) — the fundamental thermodynamical approach to predict contrail formation — with a new aircraft exhaust
600 plume detection algorithm to statistically discriminate between the contrail and natural cirrus measured above Central Europe during the ML-CIRRUS research aircraft campaign in Spring 2014.

Cloud particles matching SAC are presumably attributed to contrail cirrus, while those missing SAC are treated as natural cirrus. Comparatively young contrail cirrus were encountered most frequently in the cruising altitude (CA) with ambient pressure ranging from 200 to 245 hPa (ambient temperature range 207–218 K). Figure 11 summarises the microphysical and
605 optical properties of the contrail and natural cirrus observed during the ML-CIRRUS. It shows that the microphysical and optical properties of the contrail (Fig. 11, left) and natural cirrus (Fig. 11, right) differ markedly with the contrail cirrus occurring in a much higher median number density $N_{ice} = 0.045 \text{ cm}^{-3}$ accompanied by a smaller mass mean radius $R_{ice} = 16.6 \text{ }\mu\text{m}$ and mostly ice water content $IWC < 10 \text{ ppmv}$, compared to $N_{ice} = 0.018 \text{ cm}^{-3}$, $R_{ice} = 42.4 \text{ }\mu\text{m}$ and IWC frequently above



610 **Figure 11.** Ice crystal number concentration N_{ice} vs. mass mean radius R_{ice} colour coded with extinction coefficient Ext (unit: km^{-1}) of ice particles. Ice water content IWC isolines in relation to N_{ice} and R_{ice} are also plotted. Left: the contrail cirrus that fulfil the Schmidt-Appleman criterion (SAC) inside the cruising altitude (CA, ambient pressure 200–245 hPa, ambient temperature 207–218 K), also identified as in situ-
615 origin cirrus; median: $N_{ice} = 0.045 \text{ cm}^{-3}$, $R_{ice} = 16.6 \text{ }\mu\text{m}$, $IWC = 3.5 \text{ ppmv}$, $Ext = \sim 0.056 \text{ km}^{-1}$. Middle: the cirrus mixture (fulfilling SAC and outside the CA range), which is a mixture of contrail cirrus, in situ- and liquid-origin natural cirrus; median: $N_{ice} = 0.038 \text{ cm}^{-3}$, $R_{ice} = 24.1 \text{ }\mu\text{m}$, $IWC = 8.3 \text{ ppmv}$, $Ext = \sim 0.096 \text{ km}^{-1}$. Right: the natural cirrus of liquid-origin (not fulfilling SAC and below the CA range); median: $N_{ice} = 0.018 \text{ cm}^{-3}$, $R_{ice} = 42.4 \text{ }\mu\text{m}$, $IWC = 21.7 \text{ ppmv}$, $Ext = \sim 0.137 \text{ km}^{-1}$. The 50% (blue) contour enclose 50% the most frequently occurring ice crystals. The total sampling hours of each cirrus dataset at 1Hz sampling frequency are inserted in the lower left corners of the figures.

10 ppmv in the natural cirrus. The relatively low extinction coefficients of the contrail cirrus (median 0.056 km^{-1} compared to
620 0.137 km^{-1} in the natural liquid-origin cirrus) reveal that the observed contrail cirrus clouds were rather optically thin,
indicating aged contrail cirrus particles. Altogether, the contrail cirrus sampled inside CA share the characteristics of in situ-
origin cirrus, in contrast to the large and optically thicker natural cirrus of liquid-origin. Cirrus clouds outside CA (Fig. 11,
middle) are a complex of in situ and liquid-origin cirrus with contrails embedded.

An important finding of this study is that the highest probability of RH_{ice} in the contrail cirrus occurs in slight ice-subsaturation,
625 centring at around 90% RH_{ice} , concurring with previous studies based on a smaller dataset of in situ measurements. The RH_{ice}
distribution in the natural cirrus agrees with the worldwide climatology compiled by Krämer et al. (2020; Fig. 7), which centres
around ice saturation at $T_{\text{amb}} > \sim 200 \text{ K}$. The existence of contrail cirrus in slightly ice subsaturated environments seems to be
surprising from the perspective of thermodynamic equilibrium, but Krämer et al. (2020) and Jensen et al. (2001) also reported
natural cirrus under subsaturated conditions. As predicted by a cirrus scenario simulated with the box model MAID, contrail
630 cirrus can persist up to over 4 h in around 90% RH_{ice} environment, which means that contrail cirrus likely plays a role in the
overall contrail radiative feedback provided that they appear frequently. An estimation of the air mass percentage with RH_{ice}
 $\geq 90\%$ in air traffic cruise regions, based on 15 years of MOZAIC RH_{ice} measurements, shows an increase by approximately
10% in comparison to the air mass percentage in the ISSRs. This suggests that we might need to lower the RH_{ice} threshold to
achieve the efficacy of contrail avoidance by rerouting aircraft. We also call for deeper investigations into the spatial coverage
635 and optical depth of the contrail cirrus in slight ice-subsaturated environments as well as the associated microphysical processes
to predicate their climate effect robustly. In turn, this will also facilitate the mitigation of aviation's climate impact by reducing
the occurrence of contrails and contrail cirrus.

Data availability. The ML-CIRRUS dataset supporting this study is available from the HALO database at [https://halo-
db.pa.op.dlr.de/mission/2](https://halo-db.pa.op.dlr.de/mission/2) (last access: 6 December 2022) (German Aerospace Center, 2022) or it may be provided by the
640 authors upon request. The IAGOS data are available through the IAGOS data portal at <https://doi.org/10.25326/20> (Boulanger,
2021).

Author contributions. YL and MK designed the study. YL carried it out and prepared the manuscript with contributions from
all co-authors. CM and UB developed and applied the plume detection algorithm to identify cirrus particles influenced by
aircraft exhaust. SR and AP analysed the pressure levels of IAGOS-MOZAIC flights over the North Atlantic and Europe and
645 provided air mass fractions at different RH_{ice} thresholds in this region observed during IAGOS-MOZAIC period. NS prepared
the particle size distribution data for calculating the frequency of ice particle sizes. MK performed the cirrus life cycle
simulation. GD and SG provided the RH_{ice} data from WALES. CV and US coordinated the ML-CIRRUS campaign.

Competing interests. Two of the co-authors are members of the editorial board of Atmospheric Chemistry and Physics.

Acknowledgement. We would like to thank Martin Zöger (DLR, Germany) for providing BAHAMAS and SHARC data from
650 ML-CIRRUS, Armin Afchine (FZJ, Germany) for NIXE data, Daniel Sauer (DLR, Germany) for aerosol data and Helmut
Ziereis (DLR, Germany) for providing NO_y data. We are grateful to Klaus Gierens (DLR, Germany) for helpful discussion.
MOZAIC/IAGOS data are created with support from the European Commission, national agencies in Germany (BMBF),
France (MESR), and the UK (NERC), and the IAGOS member institutions (<http://www.iagos.org/partners>). The participating
655 airlines (Deutsche Lufthansa, Air France, China Airlines, Iberia, Cathay Pacific, Hawaiian Airlines, Air Namibia, Sabena,
Austrian) supported IAGOS by carrying the measurement equipment free of charge since 1994. The data are available at
<https://doi.org/10.25326/20> thanks to additional support from AERIS. MK thanks JGU Mainz for support as a GFK fellow.
CV was funded by the Helmholtz excellence program (grant number W2/W3-060) and by the German Research Foundation
DFG in SPP 1294 HALO under contract VO 1504/7-1 and the TRR 301 – Project-ID 428312742.

Financial support. This research has been supported by the EU Horizon 2020 project Advancing the Science for Aviation
660 and ClimAte (ACACIA grant No. 875036 and the German Ministry for Education and Research (BMBF grant No.
01LK1301A).

The article processing charges for this open-access publication were covered by a Research Centre of the Helmholtz
Association.

References

- 665 Afchine, A., Rolf, C., Costa, A., Spelten, N., Riese, M., Buchholz, B., Ebert, V., Heller, R., Kaufmann, S., Minikin, A., Voigt,
C., Zöger, M., Smith, J., Lawson, P., Lykov, A., Khaykin, S., and Krämer, M.: Ice particle sampling from aircraft – influence
of the probing position on the ice water content, Atmos. Meas. Tech., 11, 4015-4031, [https://doi.org/10.5194/amt-11-4015-](https://doi.org/10.5194/amt-11-4015-2018)
[2018](https://doi.org/10.5194/amt-11-4015-2018), 2018.
- Appleman, H.: The Formation of Exhaust Condensation Trails by Jet Aircraft, Bull. Amer. Meteorol. Soc., 34, 14-20,
670 <https://doi.org/10.1175/1520-0477-34.1.14>, 1953.
- Boulangier, D.: IAGOS data portal, available at: <http://www.iagos-data.fr> (last access: 6 September 2022),
<https://doi.org/10.25326/20>, 2021.
- Bräuer, T., Voigt, C., Sauer, D., Kaufmann, S., Hahn, V., Scheibe, M., Schlager, H., Diskin, G. S., Nowak, J. B., Digangi, J.
P., Huber, F., Moore, R. H., and Anderson, B. E.: Airborne Measurements of Contrail Ice Properties—Dependence on
675 Temperature and Humidity, Geophys. Res. Lett., 48, <https://doi.org/10.1029/2020gl092166>, 2021.
- Bunz, H., Benz, S., Gensch, I., and Krämer, M.: MAID: a model to simulate UT/LS aerosols and ice clouds, Environ. Res.
Lett., 3, 035001, <https://doi.org/10.1088/1748-9326/3/3/035001>, 2008.

- Burkhardt, U. and Kärcher, B.: Global radiative forcing from contrail cirrus, *Nat. Clim. Chang.*, 1, 54-58, <https://doi.org/10.1038/nclimate1068>, 2011.
- 680 Burkhardt, U., Bock, L., and Bier, A.: Mitigating the contrail cirrus climate impact by reducing aircraft soot number emissions, *npj Clim. Atmos. Sci.*, 1, 37, <https://doi.org/10.1038/s41612-018-0046-4>, 2018.
- Burkhardt, U., Kärcher, B., and Schumann, U.: Global modeling of the contrail and contrail cirrus climate impact, *Bull. Amer. Meteorol. Soc.*, 91, 479-484, <https://doi.org/10.1175/2009BAMS2656.1> 2010.
- Chauvigné, A., Jourdan, O., Schwarzenboeck, A., Gourbeyre, C., Gayet, J. F., Voigt, C., Schlager, H., Kaufmann, S.,
- 685 Borrmann, S., Molleker, S., Minikin, A., Jurkat, T., and Schumann, U.: Statistical analysis of contrail to cirrus evolution during the Contrail and Cirrus Experiment (CONCERT), *Atmos. Chem. Phys.*, 18, 9803-9822, <https://doi.org/10.5194/acp-18-9803-2018>, 2018.
- Dee, D. P., Uppala, S. M., Simmons, A. J., Berrisford, P., Poli, P., Kobayashi, S., Andrae, U., Balmaseda, M. A., Balsamo, G., Bauer, P., Bechtold, P., Beljaars, A. C. M., van de Berg, L., Bidlot, J., Bormann, N., Delsol, C., Dragani, R., Fuentes, M.,
- 690 Geer, A. J., Haimberger, L., Healy, S. B., Hersbach, H., Hólm, E. V., Isaksen, I., Kållberg, P., Köhler, M., Matricardi, M., McNally, A. P., Monge-Sanz, B. M., Morcrette, J.-J., Park, B.-K., Peubey, C., de Rosnay, P., Tavolato, C., Thépaut, J.-N., and Vitart, F.: The ERA-Interim reanalysis: configuration and performance of the data assimilation system, *Q. J. R. Meteorol. Soc.*, 137, 553-597, <https://doi.org/10.1002/qj.828>, 2011.
- Diao, M., Zondlo, M. A., Heymsfield, A. J., Avallone, L. M., Paige, M. E., Beaton, S. P., Campos, T., and Rogers, D. C.:
- 695 Cloud-scale ice-supersaturated regions spatially correlate with high water vapor heterogeneities, *Atmos. Chem. Phys.*, 14, 2639-2656, <https://doi.org/10.5194/acp-14-2639-2014>, 2014.
- Diao, M. H., Bryan, G. H., Morrison, H., and Jensen, J. B.: Ice Nucleation Parameterization and Relative Humidity Distribution in Idealized Squall-Line Simulations, *J. Atmos. Sci.*, 74, 2761-2787, <https://doi.org/10.1175/JAS-D-16-0356.1>, 2017.
- Gayet, J.-F., Ovarlez, J., Shcherbakov, V., Ström, J., Schumann, U., Minikin, A., Auriol, F., Petzold, A., and Monier, M.:
- 700 Cirrus cloud microphysical and optical properties at southern and northern midlatitudes during the INCA experiment, *J. Geophys. Res.-Atmos.*, 109, <https://doi.org/10.1029/2004JD004803>, 2004.
- Gayet, J. F., Shcherbakov, V., Voigt, C., Schumann, U., Schäuble, D., Jessberger, P., Petzold, A., Minikin, A., Schlager, H., Dubovik, O., and Lapyonok, T.: The evolution of microphysical and optical properties of an A380 contrail in the vortex phase, *Atmos. Chem. Phys.*, 12, 6629-6643, <https://doi.org/10.5194/acp-12-6629-2012>, 2012.
- 705 German Aerospace Center: HALO database, available at: <https://halo-db.pa.op.dlr.de/mission/2>, (last access: 6 December 2022), <http://doi.org/10.17616/R39Q0T>, 2022.
- Gierens, K.: Selected topics on the interaction between cirrus clouds and embedded contrails, *Atmos. Chem. Phys.*, 12, 11943-11949, <https://doi.org/10.5194/acp-12-11943-2012>, 2012.
- Gierens, K. and Vázquez-Navarro, M.: Statistical analysis of contrail lifetimes from a satellite perspective, *Meteorol. Z.*, 27,
- 710 183-193, <https://doi.org/10.1127/metz/2018/0888>, 2018.

- Gierens, K., Matthes, S., and Rohs, S.: How Well Can Persistent Contrails Be Predicted?, *Aerospace*, 7, 169, <https://doi.org/10.3390/aerospace7120169>, 2020.
- Giez, A., Mallaun, C., Zöger, M., Dörnbrack, A., and Schumann, U.: Static Pressure from Aircraft Trailing-Cone Measurements and Numerical Weather-Prediction Analysis, *J. Aircr.*, 54, 1728-1737, <https://doi.org/10.2514/1.C034084>, 2017.
- Grewe, V., Gangoli Rao, A., Grönstedt, T., Xisto, C., Linke, F., Melkert, J., Middel, J., Ohlenforst, B., Blakey, S., Christie, S., Matthes, S., and Dahlmann, K.: Evaluating the climate impact of aviation emission scenarios towards the Paris agreement including COVID-19 effects, *Nat. Commun.*, 12, 3841, <https://doi.org/10.1038/s41467-021-24091-y>, 2021.
- Groß, S., Wirth, M., Schäfler, A., Fix, A., Kaufmann, S., and Voigt, C.: Potential of airborne lidar measurements for cirrus cloud studies, *Atmos. Meas. Tech.*, 7, 2745-2755, <https://doi.org/10.5194/amt-7-2745-2014>, 2014.
- Jensen, E. J., Toon, O. B., Kinne, S., Sachse, G. W., Anderson, B. E., Chan, K. R., Twohy, C. H., Gandrud, B., Heymsfield, A., and Miake-Lye, R. C.: Environmental conditions required for contrail formation and persistence, *J. Geophys. Res.-Atmos.*, 103, 3929-3936, <https://doi.org/10.1029/97JD02808>, 1998.
- Jensen, E. J., Toon, O. B., Vay, S. A., Ovarlez, J., May, R., Bui, T. P., Twohy, C. H., Gandrud, B. W., Pueschel, R. F., and Schumann, U.: Prevalence of ice-supersaturated regions in the upper troposphere: Implications for optically thin ice cloud formation, *J. Geophys. Res.-Atmos.*, 106, 17253-17266, <https://doi.org/10.1029/2000jd900526>, 2001.
- Jeßberger, P., Voigt, C., Schumann, U., Sölch, I., Schlager, H., Kaufmann, S., Petzold, A., Schäuble, D., and Gayet, J. F.: Aircraft type influence on contrail properties, *Atmos. Chem. Phys.*, 13, 11965-11984, <https://doi.org/10.5194/acp-13-11965-2013>, 2013.
- Kärcher, B.: Formation and radiative forcing of contrail cirrus, *Nat. Commun.*, 9, 1824, <https://doi.org/10.1038/s41467-018-04068-0>, 2018.
- Kaufmann, S., Voigt, C., Heller, R., Jurkat-Witschas, T., Krämer, M., Rolf, C., Zöger, M., Giez, A., Buchholz, B., Ebert, V., Thornberry, T., and Schumann, U.: Intercomparison of midlatitude tropospheric and lower-stratospheric water vapor measurements and comparison to ECMWF humidity data, *Atmos. Chem. Phys.*, 18, 16729-16745, <https://doi.org/10.5194/acp-18-16729-2018>, 2018.
- Klöwer, M., Allen, M. R., Lee, D. S., Proud, S. R., Gallagher, L., and Skowron, A.: Quantifying aviation's contribution to global warming, *Environ. Res. Lett.*, 16, 104027, <https://doi.org/10.1088/1748-9326/ac286e>, 2021.
- Koop, T., Luo, B., Tsias, A., and Peter, T.: Water activity as the determinant for homogeneous ice nucleation in aqueous solutions, *Nature*, 406, 611-614, <https://doi.org/10.1038/35020537>, 2000.
- Korolev, A. V. and Mazin, I. P.: Supersaturation of water vapor in clouds, *J. Atmos. Sci.*, 60, 2957-2974, [https://doi.org/10.1175/1520-0469\(2003\)060<2957:Sowvic>2.0.Co;2](https://doi.org/10.1175/1520-0469(2003)060<2957:Sowvic>2.0.Co;2), 2003.
- Krämer, M., Rolf, C., Luebke, A., Afchine, A., Spelten, N., Costa, A., Meyer, J., Zöger, M., Smith, J., Herman, R. L., Buchholz, B., Ebert, V., Baumgardner, D., Borrmann, S., Klingebiel, M., and Avallone, L.: A microphysics guide to cirrus clouds – Part 1: Cirrus types, *Atmos. Chem. Phys.*, 16, 3463-3483, <https://doi.org/10.5194/acp-16-3463-2016>, 2016.

- 745 Krämer, M., Rolf, C., Spelten, N., Afchine, A., Fahey, D., Jensen, E., Khaykin, S., Kuhn, T., Lawson, P., Lykov, A., Pan, L. L., Riese, M., Rollins, A., Stroh, F., Thornberry, T., Wolf, V., Woods, S., Spichtinger, P., Quaas, J., and Sourdeval, O.: A microphysics guide to cirrus – Part 2: Climatologies of clouds and humidity from observations, *Atmos. Chem. Phys.*, 20, 12569-12608, <https://doi.org/10.5194/acp-20-12569-2020>, 2020.
- Krautstrunk, M. and Giez, A.: The Transition From FALCON to HALO Era Airborne Atmospheric Research, in, Springer
750 Berlin Heidelberg, 609-624, https://doi.org/10.1007/978-3-642-30183-4_37, 2012.
- Kübbeler, M., Hildebrandt, M., Meyer, J., Schiller, C., Hamburger, T., Jurkat, T., Minikin, A., Petzold, A., Rautenhaus, M., Schlager, H., Schumann, U., Voigt, C., Spichtinger, P., Gayet, J. F., Gourbeyre, C., and Krämer, M.: Thin and subvisible cirrus and contrails in a subsaturated environment, *Atmos. Chem. Phys.*, 11, 5853-5865, <https://doi.org/10.5194/acp-11-5853-2011>, 2011.
- 755 Lee, D. S., Fahey, D. W., Forster, P. M., Newton, P. J., Wit, R. C. N., Lim, L. L., Owen, B., and Sausen, R.: Aviation and global climate change in the 21st century, *Atmos. Environ.*, 43, 3520-3537, <https://doi.org/10.1016/j.atmosenv.2009.04.024>, 2009.
- Lee, D. S., Fahey, D. W., Skowron, A., Allen, M. R., Burkhardt, U., Chen, Q., Doherty, S. J., Freeman, S., Forster, P. M., Fuglestad, J., Gettelman, A., De León, R. R., Lim, L. L., Lund, M. T., Millar, R. J., Owen, B., Penner, J. E., Pitari, G.,
760 Prather, M. J., Sausen, R., and Wilcox, L. J.: The contribution of global aviation to anthropogenic climate forcing for 2000 to 2018, *Atmos. Environ.*, 244, 117834, <https://doi.org/10.1016/j.atmosenv.2020.117834>, 2021.
- Luebke, A. E., Afchine, A., Costa, A., Grooß, J. U., Meyer, J., Rolf, C., Spelten, N., Avallone, L. M., Baumgardner, D., and Krämer, M.: The origin of midlatitude ice clouds and the resulting influence on their microphysical properties, *Atmos. Chem. Phys.*, 16, 5793-5809, <https://doi.org/10.5194/acp-16-5793-2016>, 2016.
- 765 Mahnke, C., Gomes, R., Bundke, U., Berg, M., Ziereis, H., Sharma, M., Righi, M., Hendricks, J., Zahn, A., and Petzold, A.: Properties and processing of aviation induced aerosol within the UTLS observed from the IAGOS-CARIBIC Flying Laboratory, EGU General Assembly 2022, Vienna, Austria., 23–27 May 2022, <https://doi.org/10.5194/egusphere-egu22-908>, 2022.
- Mallaun, C., Giez, A., and Baumann, R.: Calibration of 3-D wind measurements on a single-engine research aircraft, *Atmos. Meas. Tech.*, 8, 3177-3196, <https://doi.org/10.5194/amt-8-3177-2015>, 2015.
770
- Marengo, A., Thouret, V. N., Philippe, Smit, H., Helten, M., Kley, D., Karcher, F., Simon, P., Law, K., Pyle, J., Poschmann, G., Von Wrede, R., Hume, C., and Cook, T.: Measurement of ozone and water vapor by Airbus in-service aircraft: The MOZAIC airborne program, an overview, *J. Geophys. Res.-Atmos.*, 103, 25631-25642, <https://doi.org/10.1029/98JD00977>, 1998.
- 775 Marjani, S., Tesche, M., Bräuer, P., Sourdeval, O., and Quaas, J.: Satellite Observations of the Impact of Individual Aircraft on Ice Crystal Number in Thin Cirrus Clouds, *Geophys. Res. Lett.*, 49, e2021GL096173, <https://doi.org/10.1029/2021GL096173>, 2022.

- Meyer, J.: Ice Crystal Measurements with the New Particle Spectrometer NIXE-CAPS, Dissertation / PhD ThesisBook, Schriften des Forschungszentrums Jülich : Energie & Umwelt / Energy & Environment, Universität Wuppertal, Jülich, 2012.
- 780 Meyer, J., Rolf, C., Schiller, C., Rohs, S., Spelten, N., Afchine, A., Zöger, M., Sitnikov, N., Thornberry, T. D., Rollins, A. W., Bozóki, Z., Tátrai, D., Ebert, V., Kühnreich, B., Mackrodt, P., Möhler, O., Saathoff, H., Rosenlof, K. H., and Krämer, M.: Two decades of water vapor measurements with the FISH fluorescence hygrometer: a review, *Atmos. Chem. Phys.*, 15, 8521-8538, <https://doi.org/10.5194/acp-15-8521-2015>, 2015.
- Murphy, D. M. and Koop, T.: Review of the vapour pressures of ice and supercooled water for atmospheric applications, *Q. J. R. Meteorol. Soc.*, 131, 1539-1565, <https://doi.org/10.1256/qj.04.94>, 2005.
- 785 Neis, P., Smit, H. G. J., Rohs, S., Bundke, U., Krämer, M., Spelten, N., Ebert, V., Buchholz, B., Thomas, K., and Petzold, A.: Quality assessment of MOZAIC and IAGOS capacitive hygrometers: insights from airborne field studies, *Tellus Ser. B-Chem. Phys. Meteorol.*, 67, 28320, <https://doi.org/10.3402/tellusb.v67.28320>, 2015.
- Niklaß, M., Grewe, V., Gollnick, V., and Dahmann, K.: Concept of climate-charged airspaces: a potential policy instrument for internalizing aviation's climate impact of non-CO2 effects, *Clim. Policy*, 21, 1066-1085, <https://doi.org/10.1080/14693062.2021.1950602>, 2021.
- 790 Patnaude, R., Diao, M. H., Liu, X. H., and Chu, S. Q.: Effects of thermodynamics, dynamics and aerosols on cirrus clouds based on in situ observations and NCAR CAM6, *Atmos. Chem. Phys.*, 21, 1835-1859, <https://doi.org/10.5194/acp-21-1835-2021>, 2021.
- 795 Petzold, A., Neis, P., Rütimann, M., Rohs, S., Berkes, F., Smit, H. G. J., Krämer, M., Spelten, N., Spichtinger, P., Nédélec, P., and Wahner, A.: Ice-supersaturated air masses in the northern mid-latitudes from regular in situ observations by passenger aircraft: vertical distribution, seasonality and tropospheric fingerprint, *Atmos. Chem. Phys.*, 20, 8157-8179, <https://doi.org/10.5194/acp-20-8157-2020>, 2020.
- Petzold, A., Busen, R., Schröder, F. P., Baumann, R., Kuhn, M., Ström, J., Hagen, D. E., Whitefield, P. D., Baumgardner, D., Arnold, F., Borrmann, S., and Schumann, U.: Near-field measurements on contrail properties from fuels with different sulfur content, *J. Geophys. Res.-Atmos.*, 102, 29867-29880, <https://doi.org/10.1029/97JD02209>, 1997.
- 800 Petzold, A., Marsh, R., Johnson, M., Miller, M., Sevcenco, Y., Delhaye, D., Ibrahim, A., Williams, P., Bauer, H., Crayford, A., Bachalo, W. D., and Raper, D.: Evaluation of Methods for Measuring Particulate Matter Emissions from Gas Turbines, *Environ. Sci. Technol.*, 45, 3562-3568, <https://doi.org/10.1021/es103969y>, 2011.
- 805 Petzold, A., Formenti, P., Baumgardner, D., Bundke, U., Coe, H., Curtius, J., DeMott, P. J., Flagan, R. C., Fiebig, M., Hudson, J. G., McQuaid, J., Minikin, A., Roberts, G. C., and Wang, J.: In Situ Measurements of Aerosol Particles, in: *Airborne Measurements for Environmental Research*, 157-223, <https://doi.org/10.1002/9783527653218.ch4>, 2013.
- Petzold, A., Krämer, M., Neis, P., Rolf, C., Rohs, S., Berkes, F., Smit, H. G. J., Gallagher, M., Beswick, K., Lloyd, G., Baumgardner, D., Spichtinger, P., Nédélec, P., Ebert, V., Buchholz, B., Riese, M., and Wahner, A.: Upper tropospheric water vapour and its interaction with cirrus clouds as seen from IAGOS long-term routine in situ observations, *Faraday Discuss.*, 200, 229-249, <https://doi.org/10.1039/C7FD00006E>, 2017.
- 810

- Petzold, A., Thouret, V., Gerbig, C., Zahn, A., Brenninkmeijer, C. A. M., Gallagher, M., Hermann, M., Pontaud, M., Ziereis, H., Boulanger, D., Marshall, J., Nédélec, P., Smit, H. G. J., Friess, U., Flaud, J.-M., Wahner, A., Cammas, J.-P., and Volz-Thomas, A.: Global-scale atmosphere monitoring by in-service aircraft – current achievements and future prospects of the European Research Infrastructure IAGOS, *Tellus Ser. B-Chem. Phys. Meteorol.*, 67, 28452, <https://doi.org/10.3402/tellusb.v67.28452>, 2015.
- Reutter, P., Neis, P., Rohs, S., and Sauvage, B.: Ice supersaturated regions: properties and validation of ERA-Interim reanalysis with IAGOS in situ water vapour measurements, *Atmos. Chem. Phys.*, 20, 787-804, <https://doi.org/10.5194/acp-20-787-2020>, 2020.
- Rolf, C., Krämer, M., Schiller, C., Hildebrandt, M., and Riese, M.: Lidar observation and model simulation of a volcanic-ash-induced cirrus cloud during the Eyjafjallajökull eruption, *Atmos. Chem. Phys.*, 12, 10281-10294, <https://doi.org/10.5194/acp-12-10281-2012>, 2012.
- Schmidt, E.: Die Entstehung von Eisnebel aus den Auspuffgasen von Flugmotoren, 1941.
- Schröder, F., Kärcher, B., Duroure, C., Ström, J., Petzold, A., Gayet, J.-F., Strauss, B., Wendling, P., and Borrmann, S.: On the Transition of Contrails into Cirrus Clouds, *J. Atmos. Sci.*, 57, 464-480, [https://doi.org/10.1175/1520-0469\(2000\)057%3C0464:OTTOCI%3E2.0.CO;2](https://doi.org/10.1175/1520-0469(2000)057%3C0464:OTTOCI%3E2.0.CO;2), 2000.
- Schumann, U.: On conditions for contrail formation from aircraft exhausts, *Meteorol. Z.*, 5, 4-23, <https://doi.org/10.1127/metz/5/1996/4>, 1996.
- Schumann, U.: A contrail cirrus prediction model, *Geosci. Model Dev.*, 5, 543-580, <https://doi.org/10.5194/gmd-5-543-2012>, 2012.
- Schumann, U.: Measurement and model data comparisons for the HALO-FAAM formation flight during EMeRGe on 17 July 2017, <https://doi.org/10.5281/zenodo.4427965>, 2021.
- Schumann, U. and Graf, K.: Aviation-induced cirrus and radiation changes at diurnal timescales, *J. Geophys. Res.-Atmos.*, 118, 2404-2421, <https://doi.org/10.1002/jgrd.50184>, 2013.
- Schumann, U. and Heymsfield, A. J.: On the Life Cycle of Individual Contrails and Contrail Cirrus, *Meteorol. Monogr.*, 58, 3.1-3.24, <https://doi.org/10.1175/amsmonographs-d-16-0005.1>, 2017.
- Schumann, U., Mayer, B., Gierens, K., Unterstrasser, S., Jessberger, P., Petzold, A., Voigt, C., and Gayet, J.-F.: Effective Radius of Ice Particles in Cirrus and Contrails, *J. Atmos. Sci.*, 68, 300-321, <https://doi.org/10.1175/2010jas3562.1>, 2011.
- Schumann, U., Arnold, F., Busen, R., Curtius, J., Kärcher, B., Kiendler, A., Petzold, A., Schlager, H., Schröder, F., and Wohlfrom, K.-H.: Influence of fuel sulfur on the composition of aircraft exhaust plumes: The experiments SULFUR 1–7, *J. Geophys. Res.-Atmos.*, 107, AAC 2-1-AAC 2-27, <https://doi.org/10.1029/2001JD000813>, 2002.
- Schumann, U., Baumann, R., Baumgardner, D., Bedka, S. T., Duda, D. P., Freudenthaler, V., Gayet, J. F., Heymsfield, A. J., Minnis, P., Quante, M., Raschke, E., Schlager, H., Vázquez-Navarro, M., Voigt, C., and Wang, Z.: Properties of individual contrails: a compilation of observations and some comparisons, *Atmos. Chem. Phys.*, 17, 403-438, <https://doi.org/10.5194/acp-17-403-2017>, 2017.

- Smit, H. G. J., Volz-Thomas, A., Helten, M., Paetz, W., and Kley, D.: An in-flight calibration method for near-real-time humidity measurements with the airborne MOZAIC sensor, *J. Atmos. Ocean. Technol.*, 25, 656-666, <https://doi.org/10.1175/2007JTECHA975.1>, 2008.
- 850 Smit, H. G. J., Rohs, S., Neis, P., Boulanger, D., Krämer, M., Wahner, A., and Petzold, A.: Technical Note: Reanalysis of upper troposphere humidity data from the MOZAIC programme for the period 1994 to 2009, *Atmos. Chem. Phys.*, 14, 13241-13255, <https://doi.org/10.5194/acp-14-13241-2014>, 2014.
- Spichtinger, P., Gierens, K., Smit, H. G. J., Ovarlez, J., and Gayet, J. F.: On the distribution of relative humidity in cirrus clouds, *Atmos. Chem. Phys.*, 4, 639-647, <https://doi.org/10.5194/acp-4-639-2004>, 2004.
- Teoh, R., Schumann, U., and Stettler, M. E. J.: Beyond Contrail Avoidance: Efficacy of Flight Altitude Changes to Minimise
855 Contrail Climate Forcing, *Aerospace*, 7, 121, <https://doi.org/10.3390/aerospace7090121>, 2020a.
- Teoh, R., Schumann, U., Majumdar, A., and Stettler, M. E. J.: Mitigating the Climate Forcing of Aircraft Contrails by Small-Scale Diversions and Technology Adoption, *Environ. Sci. Technol.*, 54, 2941-2950, <https://doi.org/10.1021/acs.est.9b05608>, 2020b.
- Teoh, R., Schumann, U., Gryspeerdt, E., Shapiro, M., Molloy, J., Koudis, G., Voigt, C., and Stettler, M. E. J.: Aviation contrail
860 climate effects in the North Atlantic from 2016 to 2021, *Atmos. Chem. Phys.*, 22, 10919-10935, <https://doi.org/10.5194/acp-22-10919-2022>, 2022.
- Unterstrasser, S. a. G., Klaus and Sölch, Ingo and Wirth, Martin: Numerical simulations of homogeneously nucleated natural cirrus and contrail-cirrus. Part 2: Interaction on local scale, *Meteorol. Z.*, 26, 643-661, <https://doi.org/10.1127/metz/2016/0780>, 2017.
- 865 Urbanek, B., Groß, S., Wirth, M., Rolf, C., Krämer, M., and Voigt, C.: High Depolarization Ratios of Naturally Occurring Cirrus Clouds Near Air Traffic Regions Over Europe, *Geophys. Res. Lett.*, 45, <https://doi.org/10.1029/2018gl079345>, 2018.
- Voigt, C., Schumann, U., Jessberger, P., Jurkat, T., Petzold, A., Gayet, J.-F., Krämer, M., Thornberry, T., and Fahey, D. W.: Extinction and optical depth of contrails, *Geophys. Res. Lett.*, 38, <https://doi.org/10.1029/2011GL047189>, 2011.
- Voigt, C., Schumann, U., Jurkat, T., Schäuble, D., Schlager, H., Petzold, A., Gayet, J. F., Krämer, M., Schneider, J., Borrmann,
870 S., Schmale, J., Jessberger, P., Hamburger, T., Lichtenstern, M., Scheibe, M., Gourbeyre, C., Meyer, J., Kübbeler, M., Frey, W., Kalesse, H., Butler, T., Lawrence, M. G., Holzäpfel, F., Arnold, F., Wendisch, M., Döpelheuer, A., Gottschaldt, K., Baumann, R., Zöger, M., Sölch, I., Rautenhaus, M., and Dörnbrack, A.: In-situ observations of young contrails – overview and selected results from the CONCERT campaign, *Atmos. Chem. Phys.*, 10, 9039-9056, <https://doi.org/10.5194/acp-10-9039-2010>, 2010.
- 875 Voigt, C., Schumann, U., Minikin, A., Abdelmonem, A., Afchine, A., Borrmann, S., Boettcher, M., Buchholz, B., Bugliaro, L., Costa, A., Curtius, J., Dollner, M., Dörnbrack, A., Dreiling, V., Ebert, V., Ehrlich, A., Fix, A., Forster, L., Frank, F., Fütterer, D., Giez, A., Graf, K., Groß, J.-U., Groß, S., Heimerl, K., Heinold, B., Hüneke, T., Järvinen, E., Jurkat, T., Kaufmann, S., Kenntner, M., Klingebiel, M., Klimach, T., Kohl, R., Krämer, M., Krisna, T. C., Luebke, A., Mayer, B., Mertes, S., Molleker, S., Petzold, A., Pfeilsticker, K., Port, M., Rapp, M., Reutter, P., Rolf, C., Rose, D., Sauer, D., Schäfler, A.,

- 880 Schlage, R., Schnaiter, M., Schneider, J., Spelten, N., Spichtinger, P., Stock, P., Walser, A., Weigel, R., Weinzierl, B.,
Wendisch, M., Werner, F., Wernli, H., Wirth, M., Zahn, A., Ziereis, H., and Zöger, M.: ML-CIRRUS: The Airborne
Experiment on Natural Cirrus and Contrail Cirrus with the High-Altitude Long-Range Research Aircraft HALO, *Bull. Amer.*
Meteor. Soc., 98, 271-288, <https://doi.org/10.1175/BAMS-D-15-00213.1>, 2017.
- Wirth, M., Fix, A., Mahnke, P., Schwarzer, H., Schrandt, F., and Ehret, G.: The airborne multi-wavelength water vapor
885 differential absorption lidar WALES: system design and performance, *Appl. Phys. B-Lasers Opt.*, 96, 201,
<https://doi.org/10.1007/s00340-009-3365-7>, 2009.
- Ziereis, H., Schlager, H., Schulte, P., van Velthoven, P. F. J., and Slemr, F.: Distributions of NO, NO_x, and NO_y in the upper
troposphere and lower stratosphere between 28 degrees and 61 degrees N during POLINAT 2, *J. Geophys. Res.-Atmos.*, 105,
3653-3664, <https://doi.org/10.1029/1999jd900870>, 2000.

890